Large-scale skin metagenomics reveals extensive prevalence, coordination, and functional adaptation of skin microbiome dermotypes across body sites

Chengchen Li[1,2*], Aarthi Ravikrishnan[1*], Indrik Wijaya[1*], Ahmad Nazri Mohamed Naim[1], Jean-Sebastien Gounot[1], Stephen Wearne[3], Yue Yuan On[1], Eliza Xin Pei Ho[1], Eileen Png[1], Junmei Samantha Kwah[1], Shree Harsha Vijaya Chandra[3], Qi Yan Ang[1], Minghao Chia[1], Ng Hui Qi Amanda[1], Srinivas Ramasamy[3], Yik Weng Yew[4,5], Marie Loh[1,4,5,6], Ruo Yan Ong[3], Faith Ng[3], Sze Han Lee[3], James Chan[3,7], The HELIOS Study team, Viduthalai Rasheedkhan Regina[3,8], Thomas Dawson[3,9#], John Chambers[5#], John Common[3,10#], Niranjan Nagarajan[1,2#]

*[1]Genome Institute of Singapore (GIS), Agency for Science, Technology and Research (A*STAR), Singapore, Republic of Singapore*

[2]Yong Loo Lin School of Medicine, National University of Singapore, Singapore, Republic of Singapore

*[3]A*STAR Skin Research Labs (A*SRL), Agency for Science, Technology and Research (A*STAR) & Skin Research Institute of Singapore (SRIS), Singapore, Republic of Singapore*

[4]National Skin Centre, National Healthcare Group, Singapore, Republic of Singapore

[5]Lee Kong Chian School of Medicine, Nanyang Technological University, Singapore, Republic of Singapore

[6]Department of Epidemiology and Biostatistics, Imperial College London, South Kensington, London, UK

*[7]A*STAR Singapore Institute of Food and Biotechnology Innovation (SIFBI), Agency for Science, Technology and Research (A*STAR), Singapore, Republic of Singapore*

[8]Singapore Centre for Environmental Life Sciences and Engineering, Nanyang Technical University, Singapore, Republic of Singapore

[9]Department of Drug Discovery, College of Pharmacy, Medical University of South Carolina, Charleston, SC, USA

[10]Translational and Clinical Research Institute and NIHR Newcastle Biomedical Research Centre, Newcastle University, Newcastle upon Tyne, UK

**Joint First Authors*

[#]Corresponding Authors

Lead Contact: nagarajann@gis.a-star.edu.sg

Abstract

While skin microbiome studies have increasingly highlighted its importance in health and disease, our understanding of inter-individual heterogeneity in structure and function remains limited, impacting the ability to develop microbiome-based stratification and therapeutics. Powered by comprehensive skin microbiome characterization in a multi-ethnic population-based cohort (>3,550 shotgun metagenomes across 18 sampling sites), we established significant undescribed inter-individual heterogeneity and the extensive prevalence of distinct microbial configurations (17 species-resolution dermotypes) in seven out of nine body sites. Combining functional *in silico* and *in vitro* studies revealed insights into how these dermotypes assemble as a function of niche-dependent microbial interactions (e.g. hypoxia-dependent inhibition of *S. hominis* by *S. epidermidis*/*M. luteus*) and metabolic resource utilization (e.g. differential galactose and histidine metabolism). Integration of demographic, skin physiological, and behavioral data further identified >30 significant associations with host attributes. Cross-site analysis revealed remarkable coordination across disparate skin regions (predictive AUC-ROC>0.8) and bilateral consistency (Pearson $\rho>0.95$), emphasizing the role of specific microbial and host factors in shaping dermotypes. Finally, we provide multiple lines of evidence that dermotype states impact the risk for skin discomfort (e.g. irritation, itch) and diseases (e.g. eczema), that when combined with our highly accurate dermotype classifiers (AUC-ROC>0.98), provide a new paradigm for understanding skin microbiome function and stratifying patients in the context of skin and other diseases.

Introduction

The skin microbiome, a diverse community of bacterial, viral, and eukaryotic microbes, plays a vital role in human health by contributing to skin barrier function, preventing pathogen colonization and infections, and maintaining immune homeostasis[1–3]. Alterations in the skin microbiome are associated with a range of common skin diseases[4–17] (e.g. eczema, acne, psoriasis) and discomforts[18–23] (e.g. itch, dryness, body odor), with a significant impact on quality of life[24]. Despite groundbreaking early studies highlighting differences in skin microbiome composition across body sites[25–28] and long-term temporal stability[29], our understanding of variability across individuals (i.e. population heterogeneity), and factors defining skin microbial ecology and function remain limited[30–33]. This knowledge is critical for developing targeted immune and microbiome therapies, and patient stratification to define disease risk, treatment response, and prognosis[34–36].

The subject of population heterogeneity and distinct microbial community types has received notable attention in body sites such as the gut and the vaginal tract. For example, in the gut, a seminal study described three distinct enterotypes—stable microbiome configurations—associated with various host factors and health[37–39]. Recent studies have sought to challenge or refine this concept further with ideas such as entero-signatures and microbial guilds, which describe distinct sets of species that co-occur variably across individuals and define host-microbe interactions[40,41]. Similarly, vaginal microbiome studies have consistently identified five distinct community types and linked them with personal hygiene, lifestyle, and reproductive health[42–46].

While gut and vaginal microbiome community types have been established as important organizing principles and risk factors relevant to host health, skin microbiome studies have yielded comparatively limited evidence. Early work based on data from the Human Microbiome Project provided initial hints into the presence of skin microbiome community types[47,48], but it relied on low-resolution bacterial 16S rRNA sequencing and lacked information on associations with microbial functions and skin phenotypes. Recent shotgun metagenomics-based studies have offered more detailed information about microbial species and functions (including key fungal species), but have been limited to single-site, disease/dysbiosis contexts[49–51] (e.g. eczema or air pollution). Correspondingly, we know little about skin microbiome community types (that we refer to as dermotypes) in the general population, and the roles that microbial and host functions play in shaping them remain unestablished. Furthermore, whether dermotypes are coordinated across the

entire skin organ system, and whether dermotype states can influence host phenotypes including skin discomfort and disease, remains unknown.

Here we address these knowledge gaps by comprehensively exploring skin microbiomes in 18 different sampling sites of a multi-ethnic cohort of 200 adults representing the general population across the spectrum of health and disease. We captured a broad range of parameters by combining shotgun metagenomic sequencing data (n=3,600 samples), demographic information (e.g., age, ethnicity, etc.), skin physiological measurements (e.g., skin pH, hydration, etc.), and extensive skin health questionnaire data (e.g., skin care and skin discomfort/disease related questions). Integrated analysis of this data revealed substantial population heterogeneity, and extensive prevalence of dermotypes across body sites (7 out of 9 sites, including five different dermotypes in the axilla). Remarkably, we discovered systemic coordination of dermotypes across physiologically distinct sites (e.g., dry forearm and sebaceous forehead), challenging the independence of site specificity in the skin microbiome and suggestive of a globally coordinated system. We derived mechanistic insights into dermotype emergence and established how microbiome-intrinsic factors, including differences in species co-abundance patterns, interspecies interactions (e.g., hypoxia-dependent inhibition of *S. hominis* by *S. epidermidis* and *M. luteus*), and microbial metabolic pathways (e.g., galactose utilization favoring *S. hominis* over *S. epidermidis*), can shape dermotype structures. Host factors such as demographics were found to be informative for dermotype prediction in only a few body sites (e.g., elbow crease, mean AUC-ROC=0.79), whereas microbial features such as metabolic functions and dermotypes from other body sites typically had greater predictive power. We trained near-perfect classifiers for dermotype labels (AUC-ROC>0.98), with as few as five species in all cases, underscoring the potential for dermotype identification with just a few signature species. Overall, this work establishes the importance of accounting for population heterogeneity in skin microbiome investigations, while highlighting specific microbial and host factors that shape dermotypes, which in turn can impact skin discomforts and diseases. We further provide a clinically actionable framework for assigning skin microbiome states to individuals, facilitating the development of patient stratification strategies and personalized treatments.

Results

Analysis of inter-individual heterogeneity in the skin microbiome identifies robust dermotype states across multiple body sites

113 To capture skin microbiome heterogeneity across individuals and different body sites in the general
114 population, we generated an extensive collection of skin samples (n=3,600) from 18 different
115 sampling sites in 200 adults recruited from the Health For Life In Singapore (HELIOS) precision
116 medicine cohort[52] (**Figure 1A**, **Supplementary Table 1**; **Methods**). The samples included the left
117 and right sides of nine sites of importance for skin health and disease[17,53,54], including scalp (Sc),
118 parietal scalp (Ps), forehead (Fo), cheek (Ch), upper back (Ub), axilla (Ax), antecubital
119 fossa/elbow crease (Ac), volar forearm (Vf), and lower leg (Ll; **Figure 1A**). A substantial fraction
120 of the samples (3,586/3,600=99.6%) were successfully and consistently processed for the
121 construction of metagenomic libraries and sequenced on an Illumina HiSeq platform to
122 generate >70 billion reads and >10Tbp of data in total (2×150bp reads, median of 21.6 million
123 reads and 3.3Gbp of data per library). The resulting metagenomic datasets were processed to filter
124 reads for quality, identify the non-human fraction (median of 7.4 million reads and 1.1Gbp per
125 library), and conduct microbial taxonomic profiling. Data from negative controls (n=46; median
126 of 7.3 million non-human reads; **Supplementary File 1**) were integrated to identify and exclude
127 contaminant taxa (**Supplementary File 2**) and remove poor quality profiles (**Supplementary**
128 **Figure 1**; **Methods**). Separately, we collected extensive participant data to investigate associations
129 between inter-individual skin microbiome variations and host factors, including demographic
130 information (age, gender, ethnicity, etc.), skin physiological measurements (sebum level, pH, etc.),
131 skin-care practice (hygiene, personal-care product usage), and skin health data (skin discomfort
132 and diseases; **Supplementary Table 1**). This collection provides the largest consistently processed
133 skin metagenome dataset for a population-wide cohort to date (n=3,572; **Supplementary File 3**),
134 enabling in-depth comparisons of the skin microbiome across individuals and analysis of its
135 implication for skin health.

136 Leveraging data availability from the left and right sides of different body sites (n=9) for
137 many individuals (n=200), we first investigated the extent to which skin microbiomes exhibit
138 bilateral symmetry, beyond observations in a few individuals[26] and sites[5,49]. Despite factors such
139 as dominant hand use and skin product usage not being symmetric, high bilateral concordance was
140 observed for most individuals across body sites (median Pearson correlation>0.95, except for
141 axilla; **Figure 1B**). At all nine body sites studied, skin microbiomes from the left and right sides
142 of the body were significantly more similar than across individuals (Wilcoxon test p-value<0.001;
143 **Figure 1B**). This pattern is robust and seen with the Yue-Clayton similarity index as well, which

144 factors in shared and non-shared species[55] (Wilcoxon test p-value<0.001, **Supplementary Figure**
145 **2A**), and after accounting for (within-sample) diversity (Shannon index, **Figure 1B**) and
146 *Cutibacterium acnes* dominance[2] as a potential confounder (Wilcoxon test p-value<0.001,
147 **Supplementary Figure 2B**; **Methods**). In the background of the high general concordance
148 observed, >14% of sites (255/1779) exhibited discordance in 121 individuals across different body
149 sites (**Supplementary Figure 3A**; **Methods**). Intriguingly, bilateral discordance was enriched in
150 some individuals (binomial test BH-adjusted p-value<0.05; **Supplementary Figure 3B**), where
151 multiple body sites exhibited correlated patterns of bilateral discordance (e.g., head sites and upper
152 back; **Supplementary Figure 3C**). Specific associations were also detected between bilateral
153 microbiome discordance and various host attributes, including gender (e.g. cheek discordance in
154 women; **Supplementary Figure 3D**), personal habits (e.g. scalp discordance and daily hair
155 covering; **Figure 1C**), and skin conditions (e.g. forehead discordance and higher itch score; **Figure**
156 **1C**). Hence, while the adult skin microbiome is established here to be strongly bilaterally
157 concordant across body sites, coordinated discordance at specific sites may be triggered by host-
158 specific differences in the skin microenvironment arising out of behavioral and/or skin condition
159 changes.

160 Aggregating skin microbiome taxonomic profiles across body sites revealed the broad
161 influence of skin microenvironment on skin microbiome composition[27,28], with profiles from the
162 same site largely clustering together, and axilla (Ax) sites with their hypoxic and moist
163 environments being the most distinct (**Supplementary Figure 4A**). While sebaceous head and
164 scalp sites (Sc, Ps, Fo, and Ch) exhibited the highest similarity, even the two most similar scalp
165 sites (Ps, Sc) had statistically significant differences in beta (between-sample) diversity
166 (PERMANOVA adonis p-value<0.05; **Supplementary Figure 4B**). Site-specific differentially
167 abundant species included enrichment in lipophilic *C. acnes* in sebaceous head sites[27], the fungus
168 *Malassezia globosa* in the elbow crease (Ac) and upper back[56] (Ub), and *Malassezia restricta* in
169 scalp sites[57,58], as well as novel observations including *Cutibacterium avidum*, *Cutibacterium*
170 *granulosum*, and various *Staphylococcus* and *Corynebacterium* species in the axilla (consistent
171 with their preference for moist environments), and *Micrococcus luteus, Moraxella osloensis*, and
172 common oral taxa (*Streptococcus pneumoniae*, *Corynebacterium matruchotii*, and *Rothia*
173 *mucilaginosa*) in the forearm (Vf) and elbow crease (Ac; **Supplementary File 4**), defining the
174 broad dimensions of skin microbes with preferences for site-specific environmental niches.

175 Despite these consistent differences across sites, we found that individual skin
176 microbiomes from a given body site often exhibit multimodal distributions across principal axes
177 of variation (e.g., Ac and Ax sites; **Supplementary Figure 4A**), suggesting substantial inter-
178 individual heterogeneity in the population. Exploiting the availability of a large number of
179 consistently processed taxonomic profiles for each site (n>395), we developed a systematic
180 clustering strategy to identify robust stratification in the data, as well as assess stability of cluster
181 membership via bootstrapping (n=100; **Supplementary Figure 5**; **Methods**). Overall, seven out
182 of nine sites (i.e. Ax, Ac, Vf, Ub, Fo, Ps, Sc) showed clear evidence for multiple robust clusters
183 we term dermotypes, with all clusters having a median stability >90%. All identified dermotypes
184 were found to have prevalence in the population >10%, with the two dermotypes identified in the
185 volar forearm both having prevalence >40%. Notably, axilla sites displayed the greatest diversity
186 with five robust dermotypes, each represented by a high-density region of samples (**Figure 1D**).
187 Additionally, we identified two dermotypes at each of the remaining sites except cheek and lower
188 leg sites, where only a single robust cluster was detected (**Supplementary Figure 6A-F**). While
189 *C. acnes*-enriched dermotypes were common (Ax-2, Ac-1, Vf-1, Ub-1, Fo-1, Ps-1, and Sc-1;
190 **Figure 1E**) and with lower diversity (except Ac-1, Wilcoxon test p-value<0.05; **Supplementary**
191 **Figure 7A**), other species including *Staphylococcus*, *Corynebacterium*, *Dermabacter,*
192 *Streptococcus*, *Finegoldia*, *Brevibacterium,* and *Rothia* were found to be dominant or differentially
193 abundant across dermotypes, highlighting their contributions to dermotype structure and function
194 (**Supplementary Figure 7B**; **Supplementary File 5**). For example, the four dermotypes in the
195 axilla were dominated either by combinations of *Corynebacterium* and *Dermabacter* species and
196 with higher α-diversity (Ax-1, Ax-4), or two different *Staphylococcal* species (*Staphylococcus*
197 *hominis* at Ax-3, *Staphylococcus epidermidis* at Ax-5) and with intermediate levels of α- diversity.
198 Similarly, the elbow crease exhibited a *Staphylococcus*-dominant dermotype (Ac-2) seen in >15%
199 of the general population, while scalp sites (Sc, Ps) exhibited an *M. restricta* enriched dermotype
200 in >25% of the population, highlighting the diversity of species contributions (**Supplementary**
201 **Figure 7B**). Of note, species-level relative abundances enabled the training of near-perfect
202 classifiers for dermotype labels (AUC-ROC>0.98) with a few key signature species, emphasizing
203 the feasibility of dermotype identification in the clinic with targeted assays (**Supplementary**
204 **Figure 7C**; **Supplementary File 6**).

205 Building on the observation that skin microbiomes are bilaterally concordant, we next
206 investigated whether dermotypes across different body sites exhibited consistent associations
207 within individuals (**Figure 1F**). Indeed, remarkably strong associations were detected between
208 dermotypes across body sites, between not just physically proximal sites (e.g., scalp and parietal
209 scalp), and those with similar physiological characteristics (e.g., scalp and forehead), but also more
210 distant sites with distinct physiology (e.g., dry volar forearm and sebaceous forehead sites; Fisher's
211 exact test adjusted p-value<0.05; **Figure 1F**). These associations are not explained by preferences
212 for specific species; for example, *Staphylococcus*-dominant dermotypes in the elbow crease and
213 axilla are negatively associated with each other (**Supplementary Figure 8A**), even though
214 *Staphylococcus* strains are known to be transmissible via skin contact[59–61]. Furthermore, no strong
215 correlations were observed for the abundance of *Staphylococcus* species between these sites
216 (**Supplementary Figure 8B**), indicating that other systemic factors play a role in the observed
217 dermotype associations. Overall, these results emphasize the presence of distinct dermotype
218 configurations across individuals and body sites, with surprisingly high levels of bilateral and
219 cross-site concordance that point to body-wide coordination of host and microbial factors shaping
220 them.

221 **Dermotype-specific core and ancillary species exhibit coordinated patterns across body sites**

222 To gain deeper insights into dermotype composition, we categorized species into dermotype-
223 specific core (with ≥50% prevalence) and ancillary (<10% prevalence, ≥3 occurrences) species
224 (**Figure 2A**; **Methods**). Across all dermotypes, this identified 15 core bacterial species from the
225 genera *Cutibacterium*, *Staphylococcus*, *Corynebacterium*, *Micrococcus,* and *Moraxella*, and two
226 core fungal species from the genus *Malassezia* (**Figure 2B**). No archaea or viruses were core
227 among the 560 species analyzed, emphasizing their sporadic distribution in the human skin
228 microbiome[29]. Each dermotype contained 2-12 core species, collectively accounting for >70% of
229 community abundance, with *C. acnes* being a universal core species across all dermotypes and
230 sites. However, most taxa were core in only some sites or dermotypes, for instance *Dermabacter*
231 *sp. HFH0086,* which was categorized as a core species in the most common dermotype in the
232 axilla (Ax-1, prevalence>77%) but rarely seen in the other dermotype (Ax-2, prevalence<2%;
233 **Figure 2B**). Even abundant species such as *S. epidermidis* and *S. hominis* were not universally
234 core, while some taxa with low relative abundances (median abundance<0.5%) were core in some
235 dermotypes (e.g., *Corynebacterium tuberculostearicum*, *Corynebacterium pseudogenitalium*,

236 *Staphylococcus caprae/capitis,* and *M. globosa*). This co-existence of high- and low-abundance
237 core species within communities suggests that their collective maintenance may arise from niche
238 partitioning or complementary functional roles, independent of an abundance effect[62] (**Figure 2B**).
239 Building on our observation of dermotype correlations between body sites (**Figure 1F**), we
240 analyzed intra-individual correlations in core species abundances across the nine skin sites. Several
241 taxa, such as *M. restricta*, *S. epidermidis,* and *C. acnes*, exhibited modest positive correlations
242 when aggregated across all sites (spanning diverse microenvironments, mean ρ=0.26), and higher
243 correlations when excluding a few sites (e.g. *M. restricta* excluding Ax, mean ρ=0.37;
244 **Supplementary Figure 9A-D**). This suggests that core species shared across skin sites are
245 coordinated body-wide within individuals, potentially mediated by mechanisms such as global
246 sebum secretion favoring lipophiles, antibiotic resistance and strain dispersal[63], or immune-driven
247 niche filtering[64,65]. In contrast, *S. hominis* showed positive correlations limited to the non-scalp
248 region (**Supplementary Figure 9E**), while *M. globosa* displayed divergent correlation patterns
249 with positive associations among facial sites (ρ=0.28), but negative correlations between the cheek
250 and upper back (ρ=-0.25; **Supplementary Figure 9F**). These heterogeneous patterns imply that
251 systemic host/microbial drivers might interact with localized environmental variations (e.g., pH,
252 humidity gradients) to modulate cross-site microbial assembly patterns.
253 The 25 ancillary species we identified were disproportionally abundant at various sites and
254 dermotypes (in some cases >50% relative abundance) despite being, by definition, not overall very
255 prevalent (<10%; **Figure 2C**; **Methods**). This group includes bacteria primarily from the
256 *Pseudomonas*, *Acinetobacter*, and *Gordonia* genera (often environmentally resilient and biofilm
257 forming[66–68]), along with bacteriophages of common skin bacteria (e.g., *Cutibacterium*,
258 *Staphylococcus*), common skin viruses (e.g., polyomavirus and human papillomavirus), and a
259 fungus (*Malassezia slooffiae*; **Figure 2C**). Nearly half of ancillary taxa (12/25=48%) showed
260 specificity to a particular dermotype; for example, *Acinetobacter pittii/calcoaceticus/nosocomialis*
261 was disproportionally abundant (median abundance>50%) only in the less prevalent forehead
262 dermotype Fo-2, indicating that ancillary taxa may be adapted to specific niches available only in
263 some individuals and microbiome configurations. This was further seen in the form of significant
264 enrichment of ancillary species across multiple body sites of many individuals (≥2 sites in 87
265 individuals, BH-adjusted Poisson binomial p-value<0.05; **Figure 2C**, **Supplementary Figure**
266 **10A**). A striking example of this is *polyomavirus HPyV6,* which was abundantly present (>10%)

267 in many skin sites of some individuals (n=3) despite being lowly abundant in the general
268 population (<0.1%; **Figure 2D**). Interestingly, we also detected co-occurrence patterns in these
269 "blooms" of ancillary species across various body sites (**Supplementary 10B**), including
270 statistically significant coordination between head and limb sites for *polyomavirus HPyV6* (cheek
271 and lower leg, scalp and forearm, Fisher's exact test p-value<0.05; **Figure 2E**). In some cases,
272 more frequent carriage of an ancillary species across body sites was also associated with host
273 attributes including ethnicity (e.g. Chinese and *Malassezia slooffiae*) and skin phenotypes (e.g.
274 itch severity and *Betapapillomavirus 2;* adjusted p-value<0.05; **Supplementary Figure 10C**).
275 These results highlight the dermotype-specific nature of core and ancillary skin microbial species,
276 their coordinated distribution across body sites within individuals, and their distinct associations
277 with host phenotypes.

278 **Species co-abundance patterns reveal dermotype-dependent microbial interactions**

279 To understand how dermotypes emerge at various skin sites, we analyzed microbial correlated
280 abundance (co-abundance) patterns with a view to gaining insights into resource competition and
281 metabolic cross-feeding interactions (**Methods**). The scale of our dataset enabled robust
282 identification of >100 species-level co-abundance relationships across the nine body sites and 17
283 distinct dermotypes (**Supplementary File 7**). These include known antagonism between *C. acnes*
284 and *S. epidermidis*[69–71], and cross-feeding interactions between *Corynebacterium* and
285 *Staphylococcal* species[72] (|r|≥0.3, CCREPE q-value<0.05; **Figure 3A**; **Supplementary Figure 11**).
286 Systematic comparison of co-abundance networks and hub species—highly connected taxa—
287 across dermotypes from the same site showed that while a core set of relationships are conserved,
288 8-48% of co-abundance relationships differed significantly between dermotypes, with highest
289 differences in the axilla and lowest in parietal scalp and forearm (Fisher's Z-test p-value<0.05;
290 **Supplementary Figure 12A**). For example, *C. acnes* and *M. luteus* abundances displayed a strong
291 negative correlation in the elbow crease dermotype Ac-1 but were positively correlated in Ac-2
292 (**Figure 3A**), emphasizing the critical context that dermotypes provide for conditional interactions
293 between skin microbial species.

294 This unexpected pattern extended to core species (significant changes in 10-68% of co-
295 abundance relationships; **Supplementary Figure 12B**), with *C. acnes* in particular frequently
296 exhibiting switched relationships across dermotypes (**Supplementary Figure 12C**). As *C. acnes*
297 is an aerotolerant anaerobe, we hypothesized that oxygen availability strongly impacts *C. acnes*

growth and metabolism, and through its interactions with other skin microbes plays a critical role in shaping dermotype structure across body sites. To explore this, we systematically conducted pairwise antagonism assays among a subset of core skin bacteria (*C. acnes*, *S. hominis*, *S. epidermidis* and *M. luteus*) under hypoxic, aerobic and mixed conditions (n=186 experiments, with triplicates; **Supplementary File 8**; **Methods**). Consistent with our co-abundance network analysis, we observed that interspecies inhibitions were often condition-specific (42% of interactions tested). They also revealed several interactions that may have *in vivo* relevance, including partial inhibition of *M. luteus* by *S. epidermidis* and *S. hominis* under aerobic conditions (that mirrored corresponding exclusion edges in *C. acnes*-depleted dermotypes, e.g. Ax-2), and *C. acnes* inhibition by *M. luteus* under mixed (but not aerobic) conditions corresponding to weaker negative correlation edges in *C. acnes*-depleted dermotypes (e.g. Ub-2; **Supplementary File 7-8**). Of particular note, *S. hominis* (the dominant species in the Ac-2 dermotype) was strongly inhibited by *S. epidermidis* and *M. luteus* under hypoxic but not aerobic conditions (**Figure 3B**, **Supplementary Figure 12D-E**). Further testing showed that the agar became alkaline (pH>7) in aerobic conditions but turned acidic under hypoxic conditions (**Supplementary File 8**), indicating that these hypoxia-dependent inhibition patterns could be mediated by acidification or fermentation-derived short-chain fatty acids[74] that are unfavorable for *S. hominis* growth. Our findings suggest that the common elbow crease dermotype (Ac-1) may represent a hypoxic niche where *C. acnes* flourishes, but *S. hominis* remains suppressed due to inhibition by other skin species. In contrast, the less common elbow crease dermotype (Ac-2) may provide a more aerobic environment enabling *S. hominis* to evade inhibition and dominate, especially with reduced growth of *C. acnes*. Consistent with this hypothesis, we noted that while *S. epidermidis* is a prevalent hub species in the Ac-1 dermotype, it is no longer so in the Ac-2 dermotype and is instead replaced by *S. hominis* as a hub (**Figure 3C**), supporting the notion that *S. hominis* is more well-adapted to the environmental niche of the Ac-2 dermotype.

Further analysis of hub nodes identified key species such as *C. pseudogenitalium* and *C. tuberculostearicum* in 4 out of 12 dermotype-specific networks, highlighting that even low-abundance community members can play a major role in determining community structure (**Figure 3C**). Lastly, we noted that several bacterial species typically found as part of commensal oral flora were network hubs for specific dermotypes in the forearm, upper back, and forehead (**Figure 3C**). Further investigation of their species correlations revealed a guild of co-abundant

329 oral bacteria such as *Veillonella parvula*, *Rothia dentocariosa*, and *Corynebacterium matruchotii*,
330 that were seen in several dermotypes and were strongly co-abundant in some (e.g. Ac-1 & Vf-2;
331 **Figure 3A**, **Supplementary Figure 11**). These species are known to form a "hedgehog" structure
332 in the supragingival biofilm, which regulates pH in response to changes in nutrient availability
333 associated with food intake[75,76]. While the co-abundance patterns in these dermotypes are
334 reminiscent of oral interactions, it remains unknown whether they perform similar pH-stabilizing
335 functions, act as transient co-colonizers, or potentially exacerbate pathogenicity on skin—
336 analogous to the role of oral microbes in gastrointestinal diseases when translocating to the gut[77,78].
337 Overall, the analysis of species co-abundance networks, supported by the scale of our datasets and
338 experimental data from pairwise antagonism assays, revealed dermotype-specific inter-species
339 interactions and switches in hub species that may be a function of the aerobicity of the environment
340 and likely play an essential role in dermotype assembly.

341 **Metabolic variations between dermotypes reflect distinct host microenvironments and**
342 **influence on skin phenotypes**

343 Based on the observation that microbes residing on skin adapt to limited nutrient availability in
344 the form of carbohydrates, lipids, and proteins present in sweat, sebum, and the stratum corneum[2,3],
345 we hypothesized that differences in metabolic functions between dermotypes of the same body site
346 could provide insights into how they assemble and interact with the host. Systematic comparisons
347 of metabolic pathways present in skin metagenomes (**Supplementary File 9**) highlighted both
348 significant differences in pathway diversity across dermotypes (**Supplementary Figure 13A;**
349 **Supplementary File 10**), as well as a large fraction of pathways (>35%) being differentially
350 abundant in at least one dermotype of a body site, particularly relating to lipid, carbohydrate, amino
351 acid, nucleotide, and energy metabolism (**Supplementary Figure 13B**). We further observed a
352 suite of metabolic pathways that, while consistently present across distinct dermotypes of a given
353 site, varied significantly in abundance. For example, enrichments in arginine, tryptophan, and
354 branched-chain amino acid biosynthesis pathways (e.g., L-isoleucine, L-valine; **Supplementary**
355 **Figure 14**), that suggest frequent microbial compensation for amino acid depletion across
356 dermotypes[79–81].

357 Focusing on key differences in microbial functions for sugar degradation, amino acid
358 utilization, and fatty acid oxidation, highlighted the strong enrichment of lactose and galactose
359 degradation pathways in the elbow crease dermotype Ac-2 (**Figure 3D**). Galactose is a common

360 component of human sweat[82] and complex stratum corneum glycoconjugates where it is released
361 by corneodesmosome degradation[83], and absorbed by skin commensals via diverse
362 phosphotransferase systems[84]. We therefore hypothesized that inter-individual differences in
363 metabolite availability may play an important role in dermotype structure. Indeed, our data
364 indicates that specific *Staphylococcus* species, particularly *S. hominis*, contribute strongly to the
365 enrichment of this pathway (LACTOSECAT-PWY, **Figure 3E**), potentially due to a competitive
366 advantage under these conditions. To test this hypothesis, we compared growth kinetics of *S.*
367 *hominis* and *S. epidermidis* in mono- and co-culture, under baseline (BHI) and galactose-
368 supplemented conditions (**Supplementary Figure 15A**). While galactose enhanced overall growth
369 in both species, *S. hominis* exhibited disproportionally greater fitness gains in co-culture (>100%
370 relative to *S. epidermidis*; **Supplementary Figure 15B**), suggesting that preferential galactose
371 metabolism by *S. hominis* can provide it a competitive edge and that host-derived metabolites
372 could shape dermotype structure.

373 Similarly, histidine, a product of epidermal filaggrin breakdown and a common amino acid
374 detected on human skin[85], can be further degraded by skin microbes[86]. We observed significant
375 variations in the L-histidine degradation pathway across dermotypes (**Supplementary Figure 14**).
376 For example, the *Cutibacterium*-dominant dermotype Ac-1 in the elbow crease exhibited
377 enrichment in the L-histidine degradation pathway, with *M. luteus* being a key contributor
378 (HISDEG-PWY; **Figure 3F**; **Supplementary Figure 16A**). Further analysis of metagenomic and
379 metabolomic data collected at the elbow crease from a separate cohort (n=100; **Methods**), showed
380 that among 20 amino acids surveyed, only histidine derivative urocanic acid (UCA) differed
381 significantly between Ac dermotypes, with Ac-1 subjects enriched for cis-UCA and depleted for
382 trans-UCA (**Supplementary Figure 16B**). This is consistent with the enrichment of *M. luteus* in
383 Ac-1, and in the key enzyme for trans-UCA degradation (urocanate hydrolase; **Supplementary**
384 **Figure 16A**). While *M. luteus* abundance on skin exhibited a marginal correlation with the levels
385 of histidine and its derivates (ρ=0.21; **Supplementary Figure 16C**), a notable growth advantage
386 was observed *in vitro* with L-histidine supplementation (20% increase in OD; **Supplementary**
387 **File 12**). Intriguingly, we also observed a negative correlation between lactose metabolism and
388 histidine catabolism pathways specific to Ac-2 subjects, potentially reflecting niche-specific usage
389 of these energy sources (**Supplementary Figure 16D**). Furthermore, the enrichment of the
390 histidine degradation pathway was negatively associated with skin sensitivity (p-value<0.05;

391 **Supplementary Figure 16E**; **Supplementary File 11**), consistent with the known
392 immunosuppressive effects of cis-urocanic acid[87]. Other microbiome functions associated with
393 host phenotypes included depletion of isoleucine biosynthesis pathway (a source of natural
394 moisturizing factor[88,89]) in the volar forearm in subjects with dry skin, as well as an age-associated
395 enrichment in the phosphopantothenate biosynthesis I pathway in the cheek (a precursor for
396 coenzyme A and essential for lipid metabolism[90]), that may compensate for reduced sebum
397 production with age[91]. Together, these findings highlight that dermotypes, beyond representing
398 mere taxonomic differences, are niches with distinct metabolic properties that can be shaped by
399 differences in host-derived nutrients, and in turn can impact host skin conditions.

400 **Dermotype distribution is associated with host factors and skin discomfort/diseases**

401 Skin microbial composition can be shaped by a combination of endogenous and exogenous host
402 factors (e.g., genetics, skin physiology, lifestyle, and skin conditions), and can in turn influence
403 some of them. We leveraged the scale of our cohort to evaluate associations between dermotypes
404 and host demographics, skin physiological measurements, >15 personal care behaviors, and >25
405 skin conditions (**Methods**). Focusing on attributes relevant to each body site, we identified >35
406 significant associations (**Supplementary File 13)**.

407 Among demographic factors, ethnicity exhibited strong associations with axilla and elbow
408 crease dermotypes. In particular, axilla dermotypes dominated by *C. acnes* (Ax-2), *S. hominis* (Ax-
409 3), and *C. kroppenstedii* (Ax-4) were significantly enriched in ethnic Malay, Chinese, and Indian
410 subjects, respectively (adjusted p-value<0.05; **Figure 4A**). In contrast, the *S. hominis*-enriched
411 elbow crease dermotype (Ac-2) was more frequent in Malay and less common in Chinese subjects
412 (adjusted p-value<0.05; **Figure 4A**). Beyond ethnicity, the *S. hominis*-enriched elbow crease
413 dermotype (Ac-2) and the *Cutibacterium*-depleted upper back dermotype (Ub-2) were
414 significantly associated with female and older subjects (adjusted p-value<0.05). Strikingly, no
415 significant demographic associations were observed for head sites (forehead, scalp, parietal scalp;
416 **Supplementary File 13**), suggesting that other factors such as localized skincare practices or
417 environmental exposures may drive dermotype distributions in these sites.

418 We next assessed if skin physiological measurements revealed distinct trends across
419 dermotypes. Of note, individuals with an *S. hominis*-enriched elbow crease dermotype (Ac-2)
420 exhibited lower forearm surface hydration (p-value<0.05; **Figure 4B**), indicating that Ac-2 may
421 arise from compromised skin barrier function. Additionally, elevated cheek sebum levels (as a

422 proxy for overall sebum production in the body) were observed in individuals with *C. acnes*-
423 enriched dermotypes at the elbow crease and the volar forearm (i.e., Ac-1, Vf-1), consistent with
424 the robust growth of *C. acnes* in sebum-rich environments. In contrast, higher cheek sebum levels
425 were associated with the *C. kroppenstedii*-enriched dermotype in the axilla (i.e., Ax-4; p-
426 value<0.05; **Figure 4B**). While both species are lipophilic[92], this divergence likely reflects
427 differences in local lipid composition and species-specific substrate preferences. More broadly, to
428 explore whether site-specific skin physiological measurements reflect body-wide intrinsic states,
429 we conducted further site-agnostic analyses. Intriguingly, we observed strong associations
430 between lower trans-epidermal water loss (TEWL) levels on the cheek and *C. acnes*-depleted
431 dermotypes in the upper back (Ub-2) and forehead (Fo-2; p-value<0.05; **Supplementary Figure**
432 **17A**). Similarly, lower TEWL on the forearm associated with the *C. acnes*-depleted parietal scalp
433 dermotype (Ps-2; p-value<0.05; **Supplementary Figure 17A**), highlighting the systemic
434 connections between skin barrier functionality and skin microbial community structure.

435 Leveraging the availability of extensive skincare routine information, we next assessed
436 their potential impact on dermotypes after accounting for relevant demographic factors (**Methods**).
437 Intriguingly, routine moisturizer use and hair treatments correlated with the *C. acnes*-depleted
438 forehead dermotype (Fo-2), while daily hair covering was associated with the *C. acnes*-depleted
439 parietal scalp dermotype (Ps-2). Similarly, routine deodorant use was positively associated with
440 the axilla dermotype Ax-2 (>55% prevalence, compared to baseline of <20%), while antiperspirant
441 use was linked to Ax-4 (>25% prevalence, compared to baseline of <15%); conversely, both
442 product uses were negatively correlated with the most common axilla dermotype Ax-1, where
443 deodorant and antiperspirant use was notably lower (11% and 5%, respectively; p-value<0.05;
444 **Figure 4C**). Consistent with the antimicrobial effects of these products, Ax-2 and Ax-4 exhibited
445 reduced alpha diversity compared to Ax-1 (**Supplementary Figure 7A**). No significant
446 associations were identified for the last time of washing or antibiotic usage in the last month for
447 any of the dermotypes across the seven skin sites (**Supplementary File 13**). These observations
448 support the notion that while specific skincare practices may partially contribute to dermotype
449 prevalence in the population for some body sites, they do not define dermotype distribution across
450 individuals.

451 Our data also provides multiple lines of evidence that suggest that dermotype states may
452 serve as biomarkers or influence risk and severity for skin discomfort and diseases (after

453 accounting for demographic factors; **Methods**). For example, individuals with the *Cutibacterium*-
454 depleted scalp dermotype (Sc-2) were significantly more likely to have suffered from dry skin in
455 the last year (>70% enriched, p-value<0.05; **Figure 4C**). Similarly, individuals with the less
456 common upper back dermotype (Ub-2) were less likely to have had acne (>40% depleted, p-
457 value<0.05), while Fo-2 individuals were more likely to have sensitive skin (>60% enriched, p-
458 value<0.05). Of note, individuals with a *Staphylococcus*-dominant elbow crease dermotype (Ac-
459 2) were significantly associated with skin sensitivity, itch severity, recent itchy skin (in the last
460 week), as well as eczema history. The association with skin sensitivity and itch was found to be
461 consistent in Ac-2 subjects even among individuals without eczema history (**Supplementary**
462 **Figure 17B-C**). To explore if there could be a causal link between dermotype state and
463 risk/severity of itch, we treated human keratinocytes with supernatants of various skin derived
464 bacterial isolates (**Methods**) and assessed pro-IL-33 levels as an important cytokine signal in
465 itch[93,94]. Strikingly, several commensal strains of *S. hominis* (5/8) and *S. epidermidis* (9/12) elicited
466 a significantly elevated pro-IL-33 response compared to controls, while others such as *M. luteus*
467 did not trigger a similar response (**Supplementary Figure 17D**). These observations support the
468 hypothesis that the Ac-2 dermotype may predispose individuals to heightened skin irritation, itch,
469 and associated diseases through the enrichment of specific *Staphylococcus* species and strains.

470 Finally, we applied machine learning models to test whether the information in host
471 attributes such as demographic data, skin physiological measurements, and questionnaire
472 responses could predict dermotype labels across body sites (**Supplementary Figure 18A**;
473 **Methods**). Machine learning models that were significantly better than random were obtained in
474 all sites except for scalp sites, with the highest classification performance observed in the elbow
475 crease (Ac random forest AUC-ROC=0.8; **Figure 4D**). Among various host attributes,
476 demographic factors emerged as the most predictive in four out of seven sites analyzed (axilla,
477 scalp, upper back, elbow crease), with ethnicity frequently being among the most important
478 features (e.g. for elbow crease; **Figure 4D**, **Supplementary Figure 18B**). In summary, our
479 findings underscore the intricate interplay between host demographics (particularly ethnicity), skin
480 physiology, skincare practices, and skin dermotypes, while highlighting the utility of dermotypes
481 as biomarkers for skin health and disease risk.

482 **Microbial metabolic function and cross-site dermotypes labels are more strongly predictive**
483 **of dermotypes**

484 Having shown that certain host attributes can predict dermotype occurrence, we wondered if
485 microbial metabolic functions could serve this purpose. To ensure predictions were not driven by
486 species-specific pathway signatures, we excluded pathways highly correlated with taxa
487 abundances (Spearman $\rho \geq 0.9$, p-value<0.05) and trained multiple classifiers (e.g. ridge regression,
488 random forests etc.) to explore key metabolic functions that could jointly predict dermotype
489 structure (**Methods**). Strikingly, very high predictive performance (AUC-ROC>0.95, ridge
490 regression) was obtained with microbial metabolic features across most body sites (**Figure 4E**).
491 Restricting this analysis to conserved pathways (prevalence≥95% across all dermotypes;
492 **Supplementary Figure 19A**), still retained strong predictive ability (**Figure 4E**). A small number
493 of highly informative pathway features were identified (**Supplementary Figure 19B**), and their
494 aggregation into metabolic superclasses highlighted the role of carboxylate degradation, amino-
495 acid degradation, carbohydrate biosynthesis, fermentation, and secondary metabolite biosynthesis
496 in being predictive of dermotype labels (**Supplementary Figure 19C**). It is noteworthy that a
497 small number of microbial metabolic functions were found to be more predictive of dermotype
498 identity than all the host attributes analyzed, emphasizing the role of microbial function and
499 ecology in determining dermotypes.

500 As dermotypes were strongly correlated across body sites (**Figure 1F**), we further
501 investigated if dermotype labels could be predicted based on taxonomic profiles from other sites.
502 Remarkably, high predictive performance was obtained in many sites (AUC-ROC>0.8, random
503 forests; **Supplementary Figure 20A**), even when only data from a single site (**Supplementary**
504 **Figure 20B-C)**, or a small number of taxa were used (best AUC-ROC=0.89; **Supplementary**
505 **Figure 20D**). Intriguingly, data from the lower leg (Ll) consistently ranked highest in feature
506 importance among top-performing classifiers, despite no robust dermotypes being discovered at
507 this site. Several species including *C. acnes*, *S. epidermidis, M. restricta*, *M. globosa,* and *M.*
508 *luteus,* consistently ranked high in terms of feature importance for dermotype classification across
509 sites (**Figure 4F**), reflecting their body-wide importance for defining dermotype structure.
510 Restricting to just dermotype labels, we again noted that cross-site labels were strongly predictive,
511 and in many cases more so than host attributes (AUC-ROC>0.84, except for Ax, Ac; **Figure 4G**).

512 Ridge classifiers that integrated cross-site dermotype labels, metabolic pathway profiles,
513 and demographic factors were used to evaluate their relative information content for dermotype
514 prediction (**Figure 4H**), obtaining uniformly high performance across all sites (AUC-ROC>0.9).

515 Notably, cross-site dermotype labels ranked highest by feature importance at the parietal scalp
516 (Ps), upper back (Ub), and volar forearm (Vf; **Figure 4H**), highlighting the importance of systemic
517 microbial assembly patterns underlying dermotype structure across body sites. Although metabolic
518 pathways were generally secondary to cross-site dermotype labels, they provided complementary
519 information and even ranked highest in terms of feature importance for the scalp (Sc), suggesting
520 that microbial metabolic capabilities may have greater influence on dermotype assembly for some
521 sites. Similarly, while demographic factors had lesser feature importance in general, they had
522 significant predictive value in select sites (e.g., elbow crease [Ac] and forehead [Fo]; **Figure 4H**).
523 Overall, our findings emphasize the unexpected strength and predictive power of dermotype
524 coordination across body sites, and the critical role of specific microbial metabolic functions and
525 host demographic factors in shaping dermotype structure and function on skin.

526 **Discussion**

527 Despite growing efforts to understand the role of the skin microbiome in skin health, population-
528 based investigations defining baseline variations and features have been limited to a few early
529 studies with small cohort sizes[27,29] (n<20). Here we present the largest-to-date metagenomic
530 characterization of skin microbiomes from multiple body sites (n=18) in a cohort study that (i) is
531 an order of magnitude larger (n=200), (ii) captures broad Asian ethnic representations of Chinese,
532 Malay, and Indian individuals, and (iii) was conducted in a geographically localized setting with
533 a tropical climate (consistent humidity levels and temperature year-round), minimizing
534 confounding effects from geography and seasonable variability[95–97]. This provides a well-powered,
535 rich dataset with consistent protocols and comprehensive mapping of skin microbiomes (n=3,572
536 metagenomes), that is complemented by detailed phenotypic information, creating a valuable
537 resource for studying skin microbial ecology and function, and its relationship with host attributes
538 and skin health.

539 Leveraging this dataset, we uncovered substantial population heterogeneity in the skin
540 microbiome by comprehensively mapping robust skin microbiome dermotypes in multiple body
541 sites (7 out of 9; **Figure 1D-E**), thus establishing dermotypes as an important paradigm for
542 population stratification in skin health studies. Our work transcends prior studies that provided
543 limited evidence for, (i) context-specific community types (e.g., eczema-associated elbow crease[49],
544 air pollution-exposed face[51]), or (ii) site-agnostic patterns that overlook key site-specific
545 differences[50]. Critically, our data supports the idea that the dermotypes identified here represent

546 distinct microbiome states in regions with higher density of support (**Figure 1D**, **Supplementary**
547 **Figure 6**), unlike the continuum described in some gut enterotype studies[98,99]. Furthermore, these
548 dermotypes exhibit differential abundances for many species rather than a single signature species
549 (**Supplementary File 6**), and yet near-perfect stratification is possible with a few marker species,
550 enabling cost-effective strategies for clinical translation (e.g. using qPCR panels). This opens up
551 many avenues for studies based on dermotype stratification. For example, the axilla demonstrates
552 striking heterogeneity that has never been described before, with evidence for at least five robust
553 dermotypes dominated by multiple *Staphylococcus* and *Corynebacterium* species. While these
554 show some associations with ethnicity, sebum levels, and underarm product usage[100], they are not
555 defined by them, and further studies are needed to understand how these dermotypes emerge and
556 influence host health (e.g. body odor[22]). Similarly, the *Staphylococcus*-dominant elbow crease
557 dermotype (Ac-2) identified here supersedes our previous results specific to atopic dermatitis
558 patients[49], defining a group of individuals that may be at a greater risk for skin sensitivity, itch,
559 and eczema, and could benefit more from microbially-targeted interventions. Our additional
560 observations of *M. luteus*-enriched dermotypes in dry sites, and *M. restricta*-enriched dermotypes
561 in sebaceous scalp regions, provide the basis for further investigation into dermotype function in
562 skin conditions such as dryness and dandruff, potentially guiding the development of new pre-,
563 pro- and postbiotic treatment strategies for these large consumer care market segments.
564 Extending beyond the long-standing view of site specificity in skin microbiomes[27,28], our
565 large multi-site study revealed remarkable cross-site correlations in dermotype patterns, even
566 between physically and physiologically distinct skin sites (e.g. dry forearm and sebaceous forehead
567 sites; **Figure 1F**). This coordination is further evident from the ability to classify dermotypes at
568 one site using information from as few as 10 species or dermotype labels from another site (**Figure**
569 **4F**), a striking observation that has not been reported before in human microbiome studies[48,65,101].
570 This cross-body site correlation of dermotypes, combined with the high bilateral concordance in
571 skin microbiomes across all 9 sites and most individuals as we establish here (**Figure 1B**,
572 **Supplementary Figure 2**), indicates a deeper systemic coordination of microbiome states across
573 the body within an individual. The observation that loss of bilateral concordance can also be
574 correlated across body sites further supports the idea that dermotype assembly is shaped by
575 coordinated influences across the body (**Supplementary Figure 3C**). There are several potential
576 explanations for dermotype coordination, including strain sharing, host factors, and microbial

577 functions. For example, correlated abundances of a few core species shared across multiple sites
578 (e.g., *C. acnes*, *S. epidermidis*, and *M. restricta*; **Figure 2B**, **Supplementary Figure 9**), perhaps
579 due to strain-specific ecological functions[102–104], may partially explain our observations. However,
580 the preference for specific species/strains alone does not fully explain the patterns observed, as
581 some taxa show no significant correlations between specific sites (e.g., *Staphylococcus* species in
582 axilla and elbow crease; **Supplementary Figure 9**). Similarly, while shared host demographic,
583 physiological or behavioral factors may partially explain dermotype assembly and thus
584 coordination (**Figure 4A-C**), our predictive models suggest that they may not be the dominant
585 explanatory factors, and that key microbial metabolic functions likely play a greater role in many
586 sites (**Figure 4H)**. Taken together, our findings establish the coordination of dermotypes across
587 body sites as an important phenomenon that needs to be considered in any model for dermotype
588 assembly, and the potential to predict dermotypes across body sites based on information for a few
589 body sites.

590 To further understand the role of microbial functions in dermotype assembly, we
591 systematically investigated interspecies interactions based on mining of dermotype-dependent co-
592 abundance patterns in our large datasets, and through pairwise antagonism assays between core
593 species. These experiments identified varying oxygen availability (shaped by skin
594 physiology[105,106]) as likely a key factor impacting interspecies interactions and dermotype
595 assembly (e.g. hypoxia-dependent *S. hominis* inhibition by *S. epidermidis* and *M. luteus*; **Figure**
596 **3B**). Such oxygen-dependent antagonism may arise from differential toxin production (e.g. *S.*
597 *epidermidis* phenol-soluble modulins produced under hypoxia[107]) or redox-sensitive metabolic
598 cross-feeding[108]. Similar modulation was also seen in a recent report of multi-species interaction
599 dynamics in healthy and dandruff scalp microbiomes[109]. In addition to oxygen gradients, nutrient
600 availability differences (e.g. lipids, carbohydrates and amino acids) may also explain the large
601 number of dermotype-specific co-abundance patterns seen in our data (**Supplementary Figure**
602 **12A-B**). For example, in sebaceous environments *C. acnes* may grow well by hydrolyzing sebum
603 triglycerides into free fatty acids and thus acidifying the skin surface. This acidification, combined
604 with lipid reduction and potential antimicrobial activities, likely contributes to the unfavorable
605 conditions seen for *M. luteus* and other skin bacteria in our data[110]. Conversely, under lipid-
606 depleted conditions, the competitive dominance of *C. acnes* may diminish (**Supplementary File**
607 **8**), while species such as *S. hominis* and *M. luteus* may leverage that availability of other nutrients,

608 such as galactose and histidine as shown here (**Figure 3E-F**), to flourish and define dermotype
609 structure based on conditional interactions. Overall, the prominence of shared microbial pathways
610 such as amino acid, carbohydrate, and nucleotide biosynthesis in our predictive models
611 (**Supplementary Figure 19**) emphasizes the role of metabolic function rather than taxonomic
612 identity in driving niche specialization, dermotype-specific microbial interactions and ecosystem
613 assembly.

614 The combination of extensive host demographic, skin physiological, behavioral, and
615 discomfort/disease data, together with skin microbiome characterization across multiple body sites
616 allowed us to not only investigate the many dimensions through which specific host attributes may
617 influence dermotype prevalence, but also the potential for dermotypes to impact host phenotypes
618 and thus serve as functional biomarkers for skin health and disease. In particular, several of our
619 observations in the *S. hominis*-dominated elbow crease dermotype (Ac-2) including associations
620 with older age, reduced surface hydration, skin sensitivity, and itch, demonstrate a bidirectional
621 interplay between microbial ecology, metabolic activities, and barrier dysfunction
622 (**Supplementary Figure 21**). Compromised skin barrier, whether due to dryness, inflammation,
623 or mechanical damage from scratching, may enhance oxygen penetration, creating aerobic
624 microenvironments where *S. hominis* escapes inhibition by *S. epidermidis* and *M. luteus*. Notably,
625 *S. hominis* may further circumvent *S. epidermidis* antagonism via galactose metabolism, which
626 disproportionately enhances its growth relative to *S. epidermidis* (**Supplementary Figure 15**).
627 Thriving under these niche conditions in the skin, *S. hominis* can exacerbate itch via IL-33
628 induction in keratinocytes, perpetuating an itch-scratch cycle that further compromises barrier
629 integrity and reinforces the aerobic conditions that favor its dominance (**Supplementary Figure**
630 **17**). In contrast, enhanced *M. luteus*-mediated histidine degradation in Ac-1 dermotypes can
631 suppress inflammation and contribute to reduced skin sensitivity in Ac-1 individuals through
632 production of immunosuppressive cis-urocanic acid. Such metabolic cross-talk between the host
633 and microbes, alongside those between microbes, underscores the complex interactions that may
634 underlie dermotype associations with skin conditions (**Supplementary Figure 21**). Future work
635 in 3D skin and animal models could help disentangle these intricate relationships and enhance our
636 understanding of dermotype contributions to various skin discomforts (e.g. skin irritation, itch,
637 malodor etc.) and skin diseases (e.g. eczema, psoriasis, acne etc.). The ability to stratify subjects
638 based on skin microbiome dermotype status could offer a convenient (non-invasive) and cost-

639 effective (based on targeted panels) approach for predicting disease risk and severity, monitoring
640 treatment response, and identifying patients who would respond to specific interventions. Our
641 finding and dermotype prediction models thus redefine the roadmap for future research into
642 therapeutic strategies for skin conditions based on microbiome-informed stratification and
643 microbiome-targeted interventions.

644 # Methods

645 ## Subject recruitment and microbiome sampling

646 Subjects were recruited as part of the Asian Skin Microbiome Programme (ASMP) sub-study for
647 the Health For Life In Singapore (HELIOS) study (https://www.healthforlife.sg/), a large
648 population-based cohort that is central to the National Precision Medicine program (NPM) in
649 Singapore. The HELIOS cohort study specifically recruits subjects to ensure that their
650 demographics accurately match that of Singapore's population, considering factors such as
651 ethnicity, age, gender and socio-economic status. Informed consent was obtained from all subjects,
652 and associated protocols for the study were approved by the NTU Institutional Review Board (IRB
653 reference number: IRB-2016-11-030). Subjects were excluded from the study if they were
654 currently pregnant, breastfeeding, had any ongoing acute illness, had recent major surgery, were
655 under the age of 30, or had any mental incapacities that would prevent them from understanding
656 and giving informed consent. Upon arrival to the HELIOS clinic, subjects were given time to
657 acclimatize to the temperature of the clinic. Following this, subjects were asked to complete a skin
658 health questionnaire. This extensive questionnaire has questions related to several topics including
659 overall skin health, skin-related medical treatments, personal care routines, product usage, lifestyle
660 habits, and finally a series of questions relating to menopause for all female subjects
661 (**Supplementary File 14**). Subjects were then moved to a climate-controlled room (temperature:
662 20-22°C; relative humidity: 40-60%) for sampling by a trained research coordinator/clinician. To
663 minimize external influences, participants were instructed to avoid application of topical products
664 to sampling and measurement areas for >12 hours prior to the measurement; to avoid washing with
665 tap water, synthetic detergents, and alkaline soaps for >2, >5, and >10 hours, respectively; and to
666 refrain from ingestion of caffeinated beverages for >3 hours before and during the study period.

667 A diverse set of body sites were chosen for skin surface sampling, based on their relevance
668 for skin health and diseases[53,17,54], importance for consumer care studies, and to capture the breadth
669 of the human skin microbiome. These consisted of nine different body sites, sampled on both the
670 left and right sides (**Figure 1A**), including: scalp (Sc), forehead (Fo), cheek (Ch), upper back,
671 (Ub), antecubital fossa (elbow crease, Ac), volar forearm (Vf), and front of lower leg (Ll), for
672 which an adhesive tape disc was used for sampling (D-Squame Standard Sampling Discs, D100,
673 CuDerm). The tape was repeatedly placed on the same location with pressure and peeled 25 times

674 to saturate discs with skin surface material. For the remaining two sites, i.e. the parietal scalp (5cm
675 above the ear, Ps) and axilla (armpit, Ax), sterile swabs (FLOQSwabs Flocked Swabs, 552C,
676 Copan) were used to sample the skin microbiome by soaking in 0.9% saline and rubbing back and
677 forth on the skin for 30 seconds. The swab-based method was selected for these sites due to its
678 greater suitability in areas with dense hair, and the established very high concordance of
679 metagenomic profiles obtained relative to tape-based sampling[5]. One tape disc or swab was
680 collected from each side (left and right) of the skin sites, giving 14 tape discs and 4 swabs per
681 subject. All collected samples were stored at -80°C before sample processing. Negative control
682 samples were collected in the form of blank tape discs (n=34) and swabs (n=12) that were
683 processed in the same way as skin samples.

684 **Skin physiological measurements**

685 All measurements were conducted in a controlled temperature (20-22°C) and humidity (relative
686 humidity 40-60%) environment after at least 20 minutes of acclimatization. Trans-epidermal water
687 loss (TEWL) was measured using a VapoMeter (Delfin) on the forearm (left or right) and on the
688 cheek (just below the left eye). pH was measured using a pH meter (Delfin) on the forearm (left
689 or right). Stratum corneum surface hydration was measured using a MoistureMeter (Delfin) on the
690 forearm (left or right). Skin sebum secretion was measured using a SebumScale (Delfin) on the
691 cheek (just below the left eye). Three consistent consecutive readings were taken for all
692 measurements and averaged.

693 **DNA extraction**

694 Genomic DNA was extracted from skin tapes and swabs using a previously established protocol[5,49],
695 with modifications to improve yield. Briefly, samples were transferred into Lysing Matrix E tubes
696 containing 500 µL of Buffer ATL (Qiagen) and subjected to bead-beating at 4 m/s for 30 seconds,
697 repeated twice, using a FastPrep-24 Automated Homogenizer (MP Biomedicals). Following
698 homogenization, tubes were centrifuged at maximum speed for 5 minutes, and 200 µL of
699 supernatant was transferred to 2 mL EZ1 sample tubes (Qiagen). Proteinase K (12 µL) was added,
700 and samples were vortexed and incubated at 56 °C for 15 minutes. DNA was then purified using
701 the EZ1 Advanced XL Instrument (Qiagen) with the EZ1 DNA Tissue Kit and eluted in 50 µL of
702 EB buffer.

703 **Construction and sequencing of metagenomic libraries**

704 Purified genomic DNA underwent NGS library construction steps using NEBNext Ultra II FS
705 DNA Library Prep Kit according to manufacturer's instructions. 26 µl of DNA added to
706 fragmentation reagents were mixed well and placed in a thermocycler for 10 mins at 37°C,
707 followed by 30 mins at 65°C to complete enzymatic fragmentation. Post fragmentation, adaptor-
708 ligation was performed using Illumina-compatible adaptors, diluted 10-fold as per kit's
709 recommendations prior to use. Post-ligation, size selection or cleanup of adaptor-ligated DNA was
710 performed using Ampure XP beads in a 7:10 beads-to-sample volume ratio. Unique barcode
711 indexes were added to each sample and amplified for 12 cycles under recommended kit conditions
712 to achieve multiplexing within a batch of samples. Finally, each library sample was assessed for
713 quality based on fragment size and concentration using the Agilent D1000 ScreenTape system.
714 Samples that passed the quality-checks were adjusted to identical concentrations employing
715 dilution and volume-adjusted pooling. The multiplexed sample pool was paired-end (2×151bp)
716 sequenced on an Illumina HiSeq X Ten system. All libraries were sequenced at the Novogene
717 sequencing facility in the Genome Institute of Singapore following standard Illumina sequencing
718 protocols.

719 **Taxonomic and functional profiling**

720 Raw Illumina sequencing reads were processed using an in-house Nextflow pipeline
721 (https://github.com/CSB5/shotgunmetagenomics-nf). Quality control and adapter trimming were
722 performed with FastQC v0.20.0 (default parameters). Human reads were removed by mapping to
723 the hg19 human reference genome using BWA-MEM (v0.7.17-r1188, default parameters), and
724 filtering with SAMtools (v1.7). Taxonomic profiling of the remaining reads was conducted with
725 MetaPhlAn2 (v2.7.7, default parameters). During sequencing data generation (2020 January),
726 MetaPhlAn3 (v3.0, 2020 April release) was tested but frequently omitted eukaryotic taxa,
727 including fungal species commonly observed and cultured from human skin; additionally,
728 MetaPhlAn4 (v4.0, 2022 April release) outputs viral profiles separately, without integration into
729 the non-viral taxonomic profile. Due to these limitations, we opted to use MetaPhlAn2 consistently
730 in this long-running project. To address the limited representation of *Malassezia* species in
731 MetaPhlAn2 (a commonly found fungal member of the human skin microbiome[58,111]), we
732 integrated results from PathoScope[112] (v2.0) for *Malassezia* species. Briefly, after human read
733 removal, we aligned the remaining reads to 14 *Malassezia* genomes (*M. furfur, M. obtusa, M.*
734 *yamatoensis, M. japonica, M. sympodialis, M. pachydermatis, M. restricta, M. globosa, M.*

735 *slooffiae, M. caprae, M. cuniculi, M. dermatis, M. equina,* and *M. nana*) downloaded from NCBI
736 using bpipe (v0.9.8.6_rc), and normalized mapped read counts by the total number of reads to
737 estimate the relative abundance of *Malassezia* species. Lastly, MetaPhlAn2 taxonomic profiles
738 (excluding *Malassezia*) were rescaled by multiplying by the proportion of reads that were not
739 mapped to *Malassezia* (calculated from PathoScope results). The rescaled MetaPhlAn2 profile and
740 PathoScope-derived *Malassezia* abundances were merged and renormalized using Total Sum
741 Scaling (TSS) to generate final taxonomic profiles (n=3,586) for downstream analyses. In addition,
742 we reannotated *Enyhydrobacter aerosaccus* as *Moraxella osloensis*, consistent with a previous
743 study showing that 99.4% of sequences labeled as *E. aerosaccus* in the MetaPhlAn2 database were
744 identified as *M. osloensis* using BLASTN against the NCBI nt database[50].

745 Sequencing data from negative control samples (n=46; **Supplementary File 1**) and
746 information from existing databases (PubMed, DISBIOME[113], MicroPhenoDB[114]) were used to
747 identify potential artifacts in the taxonomic profiles, particularly *kitome* species derived from DNA
748 extraction kits and sequencing reagents (**Supplementary Figure 1**). In the first tier, species
749 commonly found in negative controls (median abundance≥0.1%) were evaluated for negative
750 correlation with library concentration, a signature of a contaminant species[115] (negative Spearman
751 correlation, p-value<0.05). These kitome candidates were then used to identify additional taxa
752 highly correlated with them, potentially also arising from contamination (Spearman ρ≥0.7, p-
753 value<0.05). The second tier refines this initial selection by restricting to genera not previously
754 reported on human skin or associated with skin disease in three different databases (PubMed,
755 DISBIOME[113], MicroPhenoDB[114]). Poor-quality profiles were removed (n=14, 0.4%; kitome total
756 abundance>50%). Kitome taxa (**Supplementary File 2**) and extremely low-abundance species
757 (relative abundance<0.1%) were excluded from taxonomic profiles (set to 0), and profiles were
758 TSS-renormalized (n=3,572; **Supplementary File 3**).

759 Functional profiles and detailed species-specific reconstructions of microbial metabolic
760 pathways (MetaCyc) were generated with HUMAnN2 (v2.8.1, default parameters). Pathways that
761 were unannotated, or highly correlated with kitome species (Spearman ρ≥0.7) were filtered out.
762 TSS-renormalized pathway abundance profiles were used for subsequent analyses (n=3,550;
763 **Supplementary File 9**). Downstream data analysis was performed in R v4.4.0 unless stated
764 otherwise.

765 **Identification of dermotypes**

766 Dermotypes were identified via a three-step protocol **(Supplementary Figure 6)**. Firstly,
767 Partitioning Around Medoid (PAM) clustering was performed using Bray-Curtis dissimilarity for
768 each site. The optimal number of clusters was determined using key indices (prediction strength,
769 silhouette index, and Calinski-Harabasz index). In cases of ambiguity (i.e., disagreement across
770 various indices), we employed Mean-Shift clustering (bandwidths determined by cross-validation)
771 to search the local maxima of kernel density estimated in PCoA space (PCoA 1-3). Next, we
772 assessed sample stability and cluster robustness via bootstrapping (n=100). Clusters were deemed
773 robust if over half of the samples were consistently grouped into the same cluster in over 90% of
774 iterations (median stability≥0.9). Only sites with at least 2 robust clusters detected were defined as
775 having distinct dermotypes for subsequent analyses. Finally, we relied on PAM to infer cluster
776 memberships for robust dermotypes, with samples with <90% stability excluded from further
777 analyses.

778 **Diversity and differential abundance analysis**

779 Metrics for α-diversity (Shannon index) and β-diversity (Bray-Curtis dissimilarity) were computed
780 using the vegan package (v2.6.4). Permutational multivariate analysis of variance
781 (PERMANOVA) was performed with Bray-Curtis dissimilarity values to quantify differences in
782 microbial compositions using the adonis2 function from vegan[2] (v2.6.4) with 1,000 permutations
783 and restrictive permutations within blocks of SubjectID. Multivariable analysis estimating which
784 microbiome attributes (species, pathways) differ significantly across comparison groups was
785 carried out using MaAsLin2 (linear model, "LOG" transformation, prevalence≥10%, BH-adjusted
786 p-value<0.05), including demographic covariates (age, gender, ethnicity) as fixed effects and
787 subject ID as a random effect when applicable.

788 **Construction of species co-abundance networks**

789 Species co-abundance networks were constructed with taxonomic profiles with high cluster
790 membership stability (≥90%) in each dermotype using the "netConstruct" function in NetCoMi[116]
791 (v1.1.0), and visualized using igraph[117]. Prevalence filtering was applied to focus on prevalent taxa
792 (≥30% for Vf, Ac, Ub, and Fo dermotypes, and ≥10% for Sc, Ps, and Ax dermotypes); this filtering
793 ensures that each network construction included at least 15 taxa, minimizing spurious findings and
794 allowing for biologically meaningful insights. Compositionally corrected Spearman ρ for each
795 species pair and corresponding p-values were obtained from CCREPE[118] (v1.34.0), and

796 downstream analysis were restricted to species pairs with strong co-abundant or co-exclusion
797 patterns in each dermotype (|ρ|>0.3, BH-adjusted p-value<0.05; **Supplementary Figure 12**).
798 Hubs were defined as species with correlation strength-weighted degree centrality above the 95th
799 percentile in each network. Differential edges between dermotypes for each skin site were
800 identified using Fisher's z-test[119] for correlation values.

801 **Antagonism co-culture assays**

802 The bacterial strains studied (*Cutibacterium acnes* 6919, *Micrococcus luteus* 10240,
803 *Staphylococcus epidermidis* 12228, and *Staphylococcus hominis* 27844) were obtained from
804 ATCC. *C. acnes* was cultured in half-strength BHI broth in an anaerobic chamber at 37°C
805 overnight with agitation, and other species were cultured under the same condition aerobically.
806 After measuring the optical density at 600 nm (OD600), each culture was diluted to OD600=0.1
807 with fresh broth (5mL total) and incubated at 37°C with agitation (220 rpm) until growing to an
808 OD that corresponds to the mid-log phase of the bacteria (i.e., *C. acnes* OD=0.6; *M. luteus* OD=1;
809 *S. epidermidis* OD=2; *S. hominis* OD=2).

810 Assay plates were prepared by dispensing 2mL of molten half-strength BHI agar into each
811 well of a 12-well plate and allowing it to solidify and dry thoroughly. Each bacterial pair was
812 assayed in triplicates, with one well per replicate. For hypoxic conditions, plates were placed in
813 compact plastic pouches with anaerobic sachets (Thermo Fisher Scientific Oxoid AnaeroGen, Cat.
814 No. AN0020D). A total of 40µL of test bacterial culture (bacteria being tested for inhibitory
815 activity; 10µL per droplet, sequentially spotted four times) was applied to each well, allowing each
816 droplet to dry before applying the next. The following day, cultures of target bacteria (bacteria to
817 be assessed for inhibition) were diluted 100× in 1× PBS (10× for *C. acnes*). A 10µL aliquot of the
818 diluted target culture was then spotted adjacent to the test bacteria in each well. The plates were
819 incubated at 37°C overnight, or two nights if the target bacteria was *C. acnes*, and clearing zones
820 were assessed the following day.

821 **Effect of galactose on *Staphylococcus* species growth**

822 The effect of galactose on the growth of *Staphylococcus* species was assessed by performing
823 monoculture and co-culture experiments with *Staphylococcus epidermidis* 12228 (SE) and
824 *Staphylococcus hominis* 27844 (SH) in Brain heart infusion (BHI) broth with and without 5%
825 galactose supplementation. Briefly, six different experimental conditions were designed: 1) BHI

826 + SE 2) BHI + SH 3) BHI + Galactose 5% + SE 4) BHI + Galactose 5% + SH 5) BHI + SE + SH
827 6) BHI + Galactose 5% + SE + SH, with two separate negative controls including, BHI and BHI
828 + Galactose 5%. Growth curve experiments were performed at 37ºC for 48h with high amplitude,
829 fast speed shaking in a 100-well Honeycomb plate (Growth Curves USA) with a working volume
830 of 200µl in each well. All the experiments were performed in quadruplicates. Optical Density (OD)
831 at 600nm measured using an automated Bioscreen C MBR (Growth Curves USA) reader at 30-
832 minute intervals was plotted to obtain growth curves.

833 Cell pellet was used for DNA extraction for qPCR analysis. Each sample was treated with
834 500µl Buffer ATL (Qiagen) in Lysing Matrix E tubes and homogenized twice at 4 m/s for 30
835 seconds using the FastPrep-24 (MP Biomedicals). After centrifugation at maximum speed for 5
836 minutes, 200µl of supernatant was transferred into 2ml EZ1 tubes (Qiagen), mixed with 12µl
837 Proteinase K, vortexed, and incubated at 56°C for 15 min. DNA was extracted in EZ1 Advanced
838 XL Instrument (Qiagen) using EZ1 DNA Tissue Kit (Qiagen) and eluted in 50µl EB buffer. DNA
839 concentration was determined using a Qubit 4 Fluorometer with the Qubit dsDNA BR Assay Kit
840 (Invitrogen). qPCR reaction mixture was prepared following the instructions in the PowerSYBR
841 Green MasterMix protocol (Applied Biosystems, Cat. No. 4368577) and 1µl of the extracted DNA
842 was used as the DNA template. Reactions were run in triplicates on a 96-well plate in ViiA 7 Real-
843 Time PCR System (Applied Biosystems) with the following cycling conditions: 95°C for 2 min;
844 40 cycles of 95°C for 15 s, 60°C for 1 min; followed by a dissociation step. Standard curves were
845 generated using gBlocks (IDT) diluted to 10^8–10^3 copies/µl. Primer and gBlock sequences used
846 for the qPCR are listed in **Supplementary File 17**.

847 **Effect of histidine on *Micrococcus luteus* growth**

848 The effect of histidine on *Micrococcus luteus* was assessed by culturing *M. luteus* in Brain heart
849 infusion (BHI) broth with and without L-histidine supplementation (50µg/ml concentration), with
850 BHI used as a negative control. Growth curve experiments were performed at 37ºC for 6 days at
851 high amplitude, normal speed shaking in a 100-well Honeycomb plate (Growth Curves USA) with
852 a working volume of 200µl in each well. All the experiments were performed in triplicates. Optical
853 Density (OD) at 600nm measured using an automated Bioscreen C MBR (Growth Curves USA)
854 reader at 30-minute intervals was plotted to obtain growth curves.

855 **Metabolomics sample collection and processing**

856 An additional cohort of 100 subjects was recruited and skin samples collected in a separate sub-
857 study of the HELIOS study for skin metagenomic and targeted metabolomic analysis of 20 amino
858 acids (Ac, elbow crease; manuscript in preparation). For metabolomics, D-Squame (D100, Clinical
859 and Derm) skin tapes were collected in the same manner as for metagenomics, except that they
860 were pushed deep into their collection tube and processed by adding 1 ml of extraction buffer per
861 tube, consisting of 0.1% formic acid in water, and 0.1µg/ml heavy isotope labelled standards. The
862 tubes were then water bath sonicated (Elma) for 15 minutes at 4°C. Following sonication, 120 µl
863 from each sample was loaded onto 96 well chimney plates (Greiner Bio-One) prior to acquisition
864 by liquid chromatography mass spectrometry (LCMS). An additional 150µl was used to determine
865 the protein concentration with the Micro BCA kit (Thermo Scientific). 96 well plates holding the
866 samples were loaded into the Vanquish LC system (Thermo Scientific), utilizing the Atlantis
867 Premier BEH C18 AX 1.7 µm, 2.1×100 mm column (Waters) before being acquired on the TSQ
868 Quantis triple quadrupole MS machine (Thermo Scientific). All data files were analyzed via the
869 software Skyline. No heavy isotope labelled standard were available for trans-urocanic acid (trans-
870 UCA), so the cis-UCA heavy isotope labelled standard was used as a proxy. Output values from
871 each sample were then normalized against their respective Micro BCA derived protein
872 concentrations. Quantified values for histidine and its key derivatives (cis- and trans-UCA) are
873 available as supporting data on FigShare (https://doi.org/10.6084/m9.figshare.28850783.v1).

874 **Dermotype associations with host attributes**

875 Samples with unstable dermotype assignments (stability<90%) were excluded for each skin site;
876 additionally, subjects with highly stable yet discordant dermotypes at the same site were excluded,
877 to enhance consistency. Associations between dermotypes and demographic or physiological data
878 was assessed in two stages. In the first stage, categorical variables were analyzed using Fisher's
879 exact test, while continuous variables were evaluated using Wilcoxon tests. Only attributes that
880 demonstrated overall statistical significance were carried forward to the second stage. In the
881 second stage, categorical variables were analyzed using Fisher's exact test in a one-versus-the-rest
882 framework, with odds ratios recorded as effect sizes; for continuous variables, pairwise Wilcoxon
883 tests were performed, and rank-biserial correlations were reported as effect sizes.

884 Associations between dermotypes and questionnaire responses were assessed using logistic
885 regression models with a one-versus-rest approach to accommodate multi-label cases (e.g., with
886 five axilla dermotypes), with Beta coefficients recorded as effect sizes. When dermotypes

887 exhibited significant associations with demographic factors in prior analyses (**Figure 4A**), these
888 factors were included as covariates in the regression model. We prioritized responses relevant to
889 the body site (e.g., underarm product usage for axilla dermotypes), and included response groups
890 with at least five observations to maintain statistical power. Questions related to specific product
891 name were excluded.

892 **Machine learning-based dermotype classification**

893 To ensure comparability across questionnaire responses, all continuous variables (e.g., itch
894 severity) were z-standardized, and categorical variables were one-hot encoded. Binary-class
895 machine learning classifiers were trained to predict the dermotype of the sample based on its own
896 metagenomic profile. A one-vs-rest strategy was employed to accommodate multi-label
897 classification (i.e., axilla dermotype classification). To address class imbalance, we employed the
898 Synthetic Minority Over-sampling Technique (SMOTE) to up-sample minority class instances[120].
899 Samples with unstable clustering membership (stability<90%) were excluded from each skin site.
900 We selected six machine learning methods based on their distinct properties, such as linear
901 and non-linear capabilities. These included decision trees, logistic regression, ridge regression,
902 random forests, support vector classifiers[121] (linear and gaussian kernel) and XGBoost[122]. Model
903 training and performance reporting utilized a nested cross-validation approach to provide an
904 unbiased performance estimate by accounting for hyperparameter selection—this involved 4-fold
905 training with 3-fold inner cross-validation for hyperparameter tuning. Tuned models were
906 evaluated on a withheld 1-fold test, and the process was repeated five times with different data
907 splits. Mean accuracy and AUC-ROC scores were reported (one-vs-rest, macro average). Using
908 the same framework as described above, we trained additional dermotype classifiers with
909 alternative input features, including: 1) the sample's metabolic pathway profile, 2) metagenomic
910 profiles from other skin sites within the same host. Further analyses were based on the best-
911 performing methods: random forests for models using metagenomic profiles, and ridge regression
912 for models using metabolic pathway profiles.
913 Random forest classifiers were further trained to assess associations between host factors
914 and dermotypes using host attributes (i.e., demographics, skin physiological parameters, and
915 questionnaire data), as they provided the best performance. Only subjects with concordant
916 dermotype labels between bilateral sites were included. Lastly, to determine the relative
917 informativeness of different feature sets for dermotype classification at a given skin site, we trained

918 an inclusive ridge classifier using three broad categories of features: demographic factors,
919 conversed metabolic pathway profiles, and dermotype labels from other skin sites. Categorical
920 values were one-hot encoded and continuous values z-standardized.

921 **Commensal *Staphylococcus* strain isolation**

922 Commensal *Staphylococcus* strains were isolated from skin swabs for 4 healthy donors across 4
923 separate body sites: antecubital fossa, axilla, cheek and scalp. Swabs were immersed in 2.5mL
924 BHI broth (Oxoid), incubated at 37°C at 210rpm for 2 hours before being spread onto TSA-SB
925 (Thermo Fisher Scientific) and Baird Parker (Oxoid) plates and incubated at 37°C for 24 hours.
926 Colonies were then picked and grown in 4ml BHI broth for 16 hours overnight at 230rpm and
927 37°C. 200µL of the cultures were spun down at 5000rpm for 5 minutes. To extract gDNA the pellet
928 was resuspended in 50µL QuickExtract (Lucigen). Bacterial suspensions were then heated to 65°C
929 for 6 minutes, briefly vortexed, then heated to 98°C for 4 minutes and briefly vortexed again. PCR
930 reactions were setup with 10µL KAPA SYBR FAST (Merck), 6.4µL nuclease free water
931 (Promega), 3µL extracted gDNA and 0.6µL primer mix. Primer mixes were specific for 4 specific
932 *Staphylococcal* species (**Supplementary File 15**). PCR was run on an AriaMx Real Time PCR
933 System (Agilent Technologies). PCR products were sent for Sanger sequencing to confirm product
934 sequences. The identified *Staphylococcal* colonies were inoculated into 4ml BHI broth and grown
935 overnight for 16 hours at 230rpm and 37°C. Optical density (OD) was measured with a
936 SpectraMax M5 Microplate Reader (Molecular Devices). Overnight cultures were then grown
937 from OD 0.1 in fresh BHI for 26 hours at 230rpm and 37°C. Final OD measurements for all strains
938 after 26 hours was normalized to OD 2.75. Bacterial cultures were spun down at 5000rpm for 5
939 minutes, pellets were discarded and supernatants stored at 4°C.

940 **Human keratinocyte cell culture and Nano-Glo HiBiT**

941 A genetically modified N/TERT keratinocyte cell-line containing a 33 nucleotide HiBiT tag
942 directly adjacent to the IL33 gene, was utilized for Nano-Glo HiBiT experiments. Keratinocytes
943 were cultured in keratinocyte serum free medium (KSFM; Gibco) supplemented with bovine
944 pituitary extract (BPE) at a final concentration of 20µg/mL, epidermal growth factor (EGF) at a
945 final concentration of 0.2ng/mL, calcium chloride at a final concentration of 300µM and 1:1000
946 penicillin-streptomycin (pen-strep; Gibco). Keratinocytes were seeded onto 96-well cell culture
947 plates (Greiner) at a density of 20,000 cells per well and grown for 24 hours in 100µL KSFM.

948 After 24 hours, KSFM was removed and the keratinocytes were cultured in 100µL KSFM with
949 either 0.2% TritonX (Merck), 5% BHI, or 5% bacterial supernatants. Keratinocytes were cultured
950 overnight for 16 hours in treatment conditions. After 16 hours of treatment on the HiBiT N/TERT
951 keratinocytes, 50µL of the KSFM was transferred to a white-bottom 96-well plate (Sigma-Aldrich)
952 and mixed with 50µL Nano-Glo HiBiT extracellular reagent. The remaining 50µL of KSFM was
953 retained on the cell culture plate with the cells and mixed with 50µL CellTitre-Glo reagent. Both
954 plates were mixed on an orbital shaker for 1 minute, and incubated for 10 minutes at room
955 temperature before luminescence was measured with a SpectraMax M5 Microplate Reader.

956 **Data availability**

957 Shotgun metagenomic sequencing data is available from the European Nucleotide Archive (ENA,
958 https://www.ebi.ac.uk/ena/browser/home) under project accession number PRJEB87291.
959 Demographic data and skin physiological measurements can be found in **Supplementary File 18**.
960 Large datasets and metabolomics data are available on Figshare at
961 https://figshare.com/projects/ASMP_Dermotype/243932. The authors of this study do not own the
962 rights to the HELIOS dataset, and this dataset is under controlled access to ensure good data
963 governance, responsible data use, and that the dataset is only used for the intended research
964 purposes in compliance with HELIOS study cohort IRB and ethics approval. Access to individual
965 level data for study participants should be submitted to the HELIOS Data Access Committee
966 (email: helios_science@ntu.edu.sg).

967 **Code availability**

968 Source code for scripts used to analyze the data are available in a GitHub project at
969 https://github.com/CSB5/ASMP_Dermotype.

970 **Acknowledgments**

971 The work is supported by funding for the Asian Skin Microbiome Programme (Industry Alignment
972 Fund Pre-Positioning – IAF-PP; H18/01/a0/16) and Asian Skin Microbiome Programme 2.0 (IAF-
973 PP H22/J1/a0/040) from the National Research Foundation, Singapore. Additional support is
974 provided by HELIOS study (IRB No. 2016-11-030), which is supported by Singapore Ministry of
975 Health's (MOH) National Medical Research Council (NMRC) under its OF-LCG funding scheme
976 (MOH-000271-00), Singapore Translational Research (STaR) funding scheme

(NMRC/StaR/0028/2017), the National Research Foundation (Singapore) through the Singapore MOH NMRC and the Precision Health Research (PRECISE) under the National Precision Medicine programme (NMRC/PRECISE/2020), National Cohorts Office through the Singapore MOH NMRC (P2022-01-03 and P2022-02-03) and intramural funding from Nanyang Technological University, Lee Kong Chian School of Medicine and the National Healthcare Group. The HELIOS study is also supported by an outstanding team of administrative and operational staff (**Supplementary File 16**). This research was supported by a National Research Foundation Investigatorship grant (NRFI09-0015) to NN. The computational work for this article was partially performed on resources of the National Supercomputing Centre, Singapore (https://www.nscc.sg) and the A*STAR Computational Resource Center. We thank all investigators, staff members and study participants who made HELIOS and ASMP studies possible.

Competing interests

The authors declare no competing interests.

991 **Figure Legends**

992 **Figure 1 | Heterogeneity of site-specific skin microbial community compositions within and**
993 **across individuals. A.** Overview of skin sampling strategy, illustrating bilateral sampling at nine
994 sites with swabs for Ps and Ax and tapes for others. **B.** Boxplots quantifying the similarity of the
995 skin microbiome within (left versus right) and between individuals across sites. Sites in the inset
996 figure for alpha diversity are presented in the same order. All p-values were calculated using the
997 one-sided Wilcoxon rank-sum test (* denotes BH-adjusted p-value<0.001). Boxplot whiskers
998 represent 1.5× interquartile range or the maximum/minimum data point within the range. **C.** Left
999 barplot comparing the percentage of subjects with their hair covered daily between those with
1000 concordant and discordant parietal scalp microbiomes between left and right body sites; right
1001 boxplot showing that individuals with discordant forehead microbiomes have significantly higher
1002 itch severity. **D**. Perspective kernel density plot of Ax microbiome PCoA results with the five red
1003 dots representing local maxima determined via Mean Shift analysis. **E.** Averaged relative
1004 abundance plots of major species ranked by median abundance for each dermotype or site, with
1005 the number of stable samples in each site and dermotype shown at the bottom. **F.** Heatmap showing
1006 significant correlations for dermotype labels across sites. The color gradient denotes log10-
1007 transformed BH-adjusted Fisher's exact test p-values, and odds ratios are annotated in the boxes
1008 where appropriate.

1009 **Figure 2 | Dermotypes are characterized by distinct core and ancillary species. A.** Overview
1010 of the general trend relating species prevalence and abundances (lower leg microbiomes as an
1011 example), and the schema to categorize species into *core species* (≥50% prevalence, in blue) and
1012 *ancillary species* (≥3 occurrences, <10% prevalence, ≥95th percentile non-zero median abundance,
1013 in orange). **B.** Core species distribution by site and dermotype, with sizes corresponding to
1014 prevalences and color intensities corresponding to non-zero median abundance. Circles with red
1015 boundaries mark species with <0.5% median abundance. **C.** Left: Ancillary species distribution
1016 and non-zero median abundance at each site and dermotype. Right: Boxplots showing the intra-
1017 individual occurrence and median abundance of each ancillary species, with the number of
1018 individuals indicated on the right (each overlaid point represents one subject). The x-axis shows
1019 the number of sites (out of nine) where a given ancillary species is observed, and the color indicates
1020 its within-subject median abundance. **D.** Stacked barcharts depicting relative abundance profiles

1021 for selected subjects with blooms of *HPyV6* across multiple sites. **E.** Significant inter-site co-
1022 abundance patterns of *HPyV6*, with the color gradient denoting log10-transformed BH-adjusted
1023 Fisher's exact test p-values.

1024 **Figure 3 | Dermotypes exhibit varied species co-abundance patterns and interactions, and**
1025 **present different metabolic niches. A.** Species co-abundance networks for dermotypes in the
1026 axilla and volar forearm, respectively. Nodes represent microbial species, sized by relative
1027 abundance and colored by microbial genera (names are bolded for hub species). Squares denote
1028 species typically present in oral cavities. Edges denote significant Spearman correlations
1029 (CCREPE $|r| \geq 0.3$, p-value<0.05): purple for positive and orange for negative correlations. Thin
1030 lines indicate shared edges, while thick solid and thick dashed lines denote differential edges with
1031 $|r| \geq 0.5$ and $0.3 \leq |r| < 0.5$, respectively. **B.** Representative agar-based antagonism co-culture assay
1032 results showing *S. epidermidis* and *M. luteus* interactions with *S. hominis* under hypoxic and
1033 aerobic conditions. **C.** Presence/absence patterns for hub species identified from species co-
1034 abundance networks across dermotypes. **D.** Selected degradation-related metabolic pathways that
1035 are differentially abundant across dermotypes. **E-F**. Boxplots depicting the variation in
1036 community-level relative abundance of, (**E**) Lactose and galactose degradation I pathway, and (**F**)
1037 L-histidine degradation I pathway between two elbow crease dermotypes (Ac-1 & Ac-2), with
1038 corresponding HUMAnN2-derived species contributions summarized in stacked barcharts. P-
1039 values for comparisons across dermotypes were calculated using a one-sided Wilcoxon rank-sum
1040 test (∗∗∗∗ denotes p−value<0.0001), and boxplot whiskers represent 1.5× interquartile range or the
1041 maximum/minimum data point.

1042 **Figure 4 | Comprehensive investigation of host attributes, same-site and cross-site intrinsic-**
1043 **microbiome factors for their ability to predict dermotype labels. A.** Heatmap depicting
1044 associations between dermotypes and host demographic factors. Effect sizes are represented as
1045 odds ratios (gender, ethnicity; Fisher's exact test) or rank-biserial correlations (age;
1046 Wilcoxon test). **B.** Boxplots displaying variations in skin physiological measurements across
1047 dermotypes. **C.** Heatmap of beta coefficients from one-versus-rest logistic regression models, with
1048 corresponding p-value labeled on each tile, showing associations between dermotypes and selected
1049 personal care behaviors and skin conditions. **D.** AUC-ROC values for dermotype classifiers using
1050 random forest models trained on multi-domain host attributes. The left panel compares feature

importance of various demographic factors for the Ac dermotype classifier. **E.** Boxplots depicting AUC-ROC values for ridge classifiers trained on different categories of metabolic pathways. **F.** Top boxplots comparing AUC-ROC values for cross-site random forest classifiers trained on the full taxonomic profile versus top 10 abundant species from a single site, with the bottom heatmap showing feature importance for the top 10 species. **G.** Top barplot showing AUC-ROC values for the best-performing cross-site dermotype classifiers trained on dermotype labels from other skin sites, with the heatmap displaying combinations of dermotype labels used for training. **H.** Feature importance comparison in an inclusive ridge classifier trained on host demographic features, cross-site dermotype labels, and conserved metabolic pathway profiles. For inter-group comparisons of continuous variables (e.g., skin physiology, AUC-ROC, feature importance), p-values were calculated using a Wilcoxon rank-sum test, and boxplot whiskers represent 1.5× interquartile range or the maximum/minimum data point. For all subfigures $*$, $**$, $***$ and $****$ denote $p-value<0.05$, 0.01, 0.001 and 0.0001, respectively.

1064 **References**

1065 1. Grice, E. A. & Segre, J. A. The skin microbiome. *Nat Rev Microbiol* **9**, 244–253 (2011).

1066 2. Byrd, A. L., Belkaid, Y. & Segre, J. A. The human skin microbiome. *Nat Rev Microbiol* **16**,
1067 143–155 (2018).

1068 3. Chen, Y. E., Fischbach, M. A. & Belkaid, Y. Skin microbiota–host interactions. *Nature* **553**,
1069 427–436 (2018).

1070 4. Kong, H. H. *et al.* Temporal shifts in the skin microbiome associated with disease flares and
1071 treatment in children with atopic dermatitis. *Genome Res* **22**, 850–859 (2012).

1072 5. Chng, K. R. *et al.* Whole metagenome profiling reveals skin microbiome-dependent
1073 susceptibility to atopic dermatitis flare. *Nat Microbiol* **1**, 16106 (2016).

1074 6. Nakatsuji, T. & Gallo, R. L. The role of the skin microbiome in atopic dermatitis. *Annals of*
1075 *Allergy, Asthma & Immunology* **122**, 263–269 (2019).

1076 7. Koh, L. F., Ong, R. Y. & Common, J. E. Skin microbiome of atopic dermatitis. *Allergology*
1077 *International* **71**, 31–39 (2022).

1078 8. Fyhrquist, N. *et al.* Microbe-host interplay in atopic dermatitis and psoriasis. *Nat Commun*
1079 **10**, 4703 (2019).

1080 9. Alekseyenko, A. V. *et al.* Community differentiation of the cutaneous microbiota in
1081 psoriasis. *Microbiome* **1**, 31 (2013).

1082 10. Tett, A. *et al.* Unexplored diversity and strain-level structure of the skin microbiome
1083 associated with psoriasis. *npj Biofilms Microbiomes* **3**, 1–12 (2017).

1084 11. Chang, H.-W. *et al.* Alteration of the cutaneous microbiome in psoriasis and potential role in
1085 Th17 polarization. *Microbiome* **6**, 1–27 (2018).

1086 12. Celoria, V. *et al.* The Skin Microbiome and Its Role in Psoriasis: A Review. *Psoriasis*
1087 *(Auckl)* **13**, 71–78 (2023).

1088 13. Fitz-Gibbon, S. *et al. Propionibacterium acnes* Strain Populations in the Human Skin
1089 Microbiome Associated with Acne. *Journal of Investigative Dermatology* **133**, 2152–2160
1090 (2013).
1091 14. Kang, D., Shi, B., Erfe, M. C., Craft, N. & Li, H. Vitamin B12 modulates the transcriptome
1092 of the skin microbiota in acne pathogenesis. *Sci Transl Med* **7**, 293ra103 (2015).
1093 15. Barnard, E., Shi, B., Kang, D., Craft, N. & Li, H. The balance of metagenomic elements
1094 shapes the skin microbiome in acne and health. *Sci Rep* **6**, 39491 (2016).
1095 16. Lee, Y. B., Byun, E. J. & Kim, H. S. Potential Role of the Microbiome in Acne: A
1096 Comprehensive Review. *J Clin Med* **8**, 987 (2019).
1097 17. Carmona-Cruz, S., Orozco-Covarrubias, L. & Sáez-de-Ocariz, M. The Human Skin
1098 Microbiome in Selected Cutaneous Diseases. *Front Cell Infect Microbiol* **12**, 834135 (2022).
1099 18. Mukherjee, S. *et al.* Sebum and Hydration Levels in Specific Regions of Human Face
1100 Significantly Predict the Nature and Diversity of Facial Skin Microbiome. *Sci Rep* **6**, 36062
1101 (2016).
1102 19. Lee, H.-J. & Kim, M. Skin Barrier Function and the Microbiome. *Int J Mol Sci* **23**, 13071
1103 (2022).
1104 20. Ho, M. *et al.* Altered skin microbiome, inflammation, and JAK/STAT signaling in Southeast
1105 Asian ichthyosis patients. *Human Genomics* **18**, 38 (2024).
1106 21. Troccaz, M. *et al.* Mapping axillary microbiota responsible for body odours using a culture-
1107 independent approach. *Microbiome* **3**, 1–15 (2015).
1108 22. Lam, T. H. *et al.* Understanding the microbial basis of body odor in pre-pubescent children
1109 and teenagers. *Microbiome* **6**, 213 (2018).

1110 23. Mogilnicka, I., Bogucki, P. & Ufnal, M. Microbiota and Malodor—Etiology and
1111 Management. *Int J Mol Sci* **21**, 2886 (2020).
1112 24. Hay, R. J. *et al.* The Global Burden of Skin Disease in 2010: An Analysis of the Prevalence
1113 and Impact of Skin Conditions. *Journal of Investigative Dermatology* **134**, 1527–1534
1114 (2014).
1115 25. Roth, R. R. & James, W. D. Microbial Ecology of the Skin. *Annu. Rev. Microbiol.* **42**, 441–
1116 464 (1988).
1117 26. Grice, E. A. *et al.* Topographical and Temporal Diversity of the Human Skin Microbiome.
1118 *Science* **324**, 1190–1192 (2009).
1119 27. Oh, J. *et al.* Biogeography and individuality shape function in the human skin metagenome.
1120 *Nature* **514**, 59–64 (2014).
1121 28. Perez, G. I. P. *et al.* Body Site Is a More Determinant Factor than Human Population
1122 Diversity in the Healthy Skin Microbiome. *PLOS ONE* **11**, e0151990 (2016).
1123 29. Oh, J., Byrd, A. L., Park, M., Kong, H. H. & Segre, J. A. Temporal Stability of the Human
1124 Skin Microbiome. *Cell* **165**, 854–866 (2016).
1125 30. Prescott, S. L. *et al.* The skin microbiome: impact of modern environments on skin ecology,
1126 barrier integrity, and systemic immune programming. *World Allergy Organization Journal*
1127 **10**, (2017).
1128 31. Dimitriu, P. A. *et al.* New Insights into the Intrinsic and Extrinsic Factors That Shape the
1129 Human Skin Microbiome. *mBio* **10**, 10.1128/mbio.00839-19 (2019).
1130 32. Callewaert, C., Ravard Helffer, K. & Lebaron, P. Skin Microbiome and its Interplay with the
1131 Environment. *Am J Clin Dermatol* **21**, 4–11 (2020).

1132 33. Skowron, K. *et al.* Human Skin Microbiome: Impact of Intrinsic and Extrinsic Factors on
1133 Skin Microbiota. *Microorganisms* **9**, 543 (2021).
1134 34. Grice, E. A. The skin microbiome: potential for novel diagnostic and therapeutic approaches
1135 to cutaneous disease. *Semin Cutan Med Surg* **33**, 98–103 (2014).
1136 35. Casterline, B. W. & Paller, A. S. Early development of the skin microbiome: therapeutic
1137 opportunities. *Pediatr Res* **90**, 731–737 (2021).
1138 36. Madaan, T. *et al.* Advances in Microbiome-Based Therapeutics for Dermatological
1139 Disorders: Current Insights and Future Directions. *Experimental Dermatology* **33**, e70019
1140 (2024).
1141 37. Arumugam, M. *et al.* Enterotypes of the human gut microbiome. *Nature* **473**, 174–180
1142 (2011).
1143 38. Wu, G. D. *et al.* Linking Long-Term Dietary Patterns with Gut Microbial Enterotypes.
1144 *Science* **334**, 105–108 (2011).
1145 39. Costea, P. I. *et al.* Enterotypes in the landscape of gut microbial community composition.
1146 *Nat Microbiol* **3**, 8–16 (2018).
1147 40. Wu, G., Zhao, N., Zhang, C., Lam, Y. Y. & Zhao, L. Guild-based analysis for understanding
1148 gut microbiome in human health and diseases. *Genome Medicine* **13**, 22 (2021).
1149 41. Frioux, C. *et al.* Enterosignatures define common bacterial guilds in the human gut
1150 microbiome. *Cell Host Microbe* **31**, 1111-1125.e6 (2023).
1151 42. Ravel, J. *et al.* Vaginal microbiome of reproductive-age women. *Proc Natl Acad Sci U S A*
1152 **108**, 4680–4687 (2011).
1153 43. Gajer, P. *et al.* Temporal Dynamics of the Human Vaginal Microbiota. *Sci Transl Med* **4**,
1154 132ra52 (2012).

1155 44. De Seta, F., Campisciano, G., Zanotta, N., Ricci, G. & Comar, M. The Vaginal Community
1156 State Types Microbiome-Immune Network as Key Factor for Bacterial Vaginosis and
1157 Aerobic Vaginitis. *Front Microbiol* **10**, 2451 (2019).
1158 45. France, M. T. *et al.* VALENCIA: a nearest centroid classification method for vaginal
1159 microbial communities based on composition. *Microbiome* **8**, 166 (2020).
1160 46. Lebeer, S. *et al.* A citizen-science-enabled catalogue of the vaginal microbiome and
1161 associated factors. *Nat Microbiol* **8**, 2183–2195 (2023).
1162 47. Zhou, Y. *et al.* Exploration of bacterial community classes in major human habitats. *Genome*
1163 *Biol* **15**, R66 (2014).
1164 48. Ding, T. & Schloss, P. D. Dynamics and associations of microbial community types across
1165 the human body. *Nature* **509**, 357–360 (2014).
1166 49. Tay, A. S. L. *et al.* Atopic dermatitis microbiomes stratify into ecologic dermotypes enabling
1167 microbial virulence and disease severity. *Journal of Allergy and Clinical Immunology* **147**,
1168 1329–1340 (2021).
1169 50. Li, Z. *et al.* Characterization of the human skin resistome and identification of two
1170 microbiota cutotypes. *Microbiome* **9**, 47 (2021).
1171 51. Leung, M. H. Y. *et al.* Skin microbiome differentiates into distinct cutotypes with unique
1172 metabolic functions upon exposure to polycyclic aromatic hydrocarbons. *Microbiome* **11**,
1173 124 (2023).
1174 52. Wang, X. *et al.* The Health for Life in Singapore (HELIOS) Study: delivering Precision
1175 Medicine research for Asian populations. 2024.05.14.24307259 Preprint at
1176 https://doi.org/10.1101/2024.05.14.24307259 (2024).

1177 53. Ferček, I. *et al.* Features of the Skin Microbiota in Common Inflammatory Skin Diseases.
1178 *Life* **11**, 962 (2021).
1179 54. Zhang, X.-E. *et al.* Microbiome: Role in Inflammatory Skin Diseases. *J Inflamm Res* **17**,
1180 1057–1082 (2024).
1181 55. Yue, J. C. & Clayton, M. K. A Similarity Measure Based on Species Proportions.
1182 *Communications in Statistics - Theory and Methods* **34**, 2123–2131 (2005).
1183 56. Theelen, B. *et al.* Malassezia ecology, pathophysiology, and treatment. *Medical Mycology*
1184 **56**, S10–S25 (2018).
1185 57. Tajima, M., Sugita, T., Nishikawa, A. & Tsuboi, R. Molecular Analysis of *Malassezia*
1186 Microflora in Seborrheic Dermatitis Patients: Comparison with Other Diseases and Healthy
1187 Subjects. *Journal of Investigative Dermatology* **128**, 345–351 (2008).
1188 58. Grice, E. A. & Dawson, T. L. Host–microbe interactions: *Malassezia* and human skin.
1189 *Current Opinion in Microbiology* **40**, 81–87 (2017).
1190 59. Fritz, S. A. *et al.* Staphylococcus aureus Colonization in Children With Community-
1191 Associated Staphylococcus aureus Skin Infections and Their Household Contacts. *Archives*
1192 *of Pediatrics & Adolescent Medicine* **166**, 551–557 (2012).
1193 60. Zhou, W. *et al.* Host-specific evolutionary and transmission dynamics shape the functional
1194 diversification of Staphylococcus epidermidis in human skin. *Cell* **180**, 454-470.e18 (2020).
1195 61. Chia, M. *et al.* Shared signatures and divergence in skin microbiomes of children with atopic
1196 dermatitis and their caregivers. *Journal of Allergy and Clinical Immunology* **150**, 894–908
1197 (2022).
1198 62. Han, G., Luong, H. & Vaishnava, S. Low abundance members of the gut microbiome exhibit
1199 high immunogenicity. *Gut Microbes* **14**, 2104086.

1200 63. Zhou, W. *et al.* Host-Specific Evolutionary and Transmission Dynamics Shape the
1201 Functional Diversification of *Staphylococcus epidermidis* in Human Skin. *Cell* **180**, 454-
1202 470.e18 (2020).
1203 64. Oh, J. *et al.* The altered landscape of the human skin microbiome in patients with primary
1204 immunodeficiencies. *Genome Res* **23**, 2103–2114 (2013).
1205 65. Zhou, X. *et al.* Longitudinal profiling of the microbiome at four body sites reveals core
1206 stability and individualized dynamics during health and disease. *Cell Host & Microbe* **32**,
1207 506-526.e9 (2024).
1208 66. Thi, M. T. T., Wibowo, D. & Rehm, B. H. A. Pseudomonas aeruginosa Biofilms. *Int J Mol*
1209 *Sci* **21**, 8671 (2020).
1210 67. Gedefie, A. *et al.* Acinetobacter baumannii Biofilm Formation and Its Role in Disease
1211 Pathogenesis: A Review. *Infect Drug Resist* **14**, 3711–3719 (2021).
1212 68. Sánchez-Suárez, J., Díaz, L., Coy-Barrera, E. & Villamil, L. Specialized Metabolism of
1213 Gordonia Genus: An Integrated Survey on Chemodiversity Combined with a Comparative
1214 Genomics-Based Analysis. *BioTech* **11**, 53 (2022).
1215 69. Christensen, G. J. M. *et al.* Antagonism between Staphylococcus epidermidis and
1216 Propionibacterium acnes and its genomic basis. *BMC Genomics* **17**, 152 (2016).
1217 70. Nakamura, K. *et al.* Short chain fatty acids produced by Cutibacterium acnes inhibit biofilm
1218 formation by Staphylococcus epidermidis. *Sci Rep* **10**, 21237 (2020).
1219 71. Ahle, C. M. *et al.* Interference and co-existence of staphylococci and Cutibacterium acnes
1220 within the healthy human skin microbiome. *Commun Biol* **5**, 1–14 (2022).
1221 72. Kwaszewska, A., Sobiś-Glinkowska, M. & Szewczyk, E. M. Cohabitation—relationships of
1222 corynebacteria and staphylococci on human skin. *Folia Microbiol* **59**, 495–502 (2014).

1223 73. Nakazono, K. *et al.* Complete sequences of epidermin and nukacin encoding plasmids from
1224 oral-derived Staphylococcus epidermidis and their antibacterial activity. *PLoS One* **17**,
1225 e0258283 (2022).
1226 74. Huang, T. Y., Jiang, Y. E. & Scott, D. A. Culturable bacteria in the entire acne lesion and
1227 short-chain fatty acid metabolites of *Cutibacterium acnes* and *Staphylococcus epidermidis*
1228 isolates. *Biochemical and Biophysical Research Communications* **622**, 45–49 (2022).
1229 75. Mark Welch, J. L., Rossetti, B. J., Rieken, C. W., Dewhirst, F. E. & Borisy, G. G.
1230 Biogeography of a human oral microbiome at the micron scale. *Proceedings of the National*
1231 *Academy of Sciences* **113**, E791–E800 (2016).
1232 76. Radaic, A. & Kapila, Y. L. The oralome and its dysbiosis: New insights into oral
1233 microbiome-host interactions. *Computational and Structural Biotechnology Journal* **19**,
1234 1335–1360 (2021).
1235 77. Gevers, D. *et al.* The Treatment-Naive Microbiome in New-Onset Crohn's Disease. *Cell*
1236 *Host & Microbe* **15**, 382–392 (2014).
1237 78. Yachida, S. *et al.* Metagenomic and metabolomic analyses reveal distinct stage-specific
1238 phenotypes of the gut microbiota in colorectal cancer. *Nat Med* **25**, 968–976 (2019).
1239 79. Kaiser, J. C. & Heinrichs, D. E. Branching Out: Alterations in Bacterial Physiology and
1240 Virulence Due to Branched-Chain Amino Acid Deprivation. *mBio* **9**, e01188-18 (2018).
1241 80. Kaiser, J. C. *et al.* Repression of branched-chain amino acid synthesis in Staphylococcus
1242 aureus is mediated by isoleucine via CodY, and by a leucine-rich attenuator peptide. *PLOS*
1243 *Genetics* **14**, e1007159 (2018).

1244 81. Joglekar, P. *et al.* Integrated genomic and functional analyses of human skin–associated
1245 *Staphylococcus* reveal extensive inter- and intra-species diversity. *Proc. Natl. Acad. Sci.*
1246 *U.S.A.* **120**, e2310585120 (2023).
1247 82. Roux, P.-F., Oddos, T. & Stamatas, G. Deciphering the Role of Skin Surface Microbiome in
1248 Skin Health: An Integrative Multiomics Approach Reveals Three Distinct Metabolite–
1249 Microbe Clusters. *Journal of Investigative Dermatology* **142**, 469-479.e5 (2022).
1250 83. Danzberger, J. *et al.* Glycan distribution and density in native skin's stratum corneum. *Skin*
1251 *Res Technol* **24**, 450–458 (2018).
1252 84. Li, Z. *et al.* Integrated Human Skin Bacteria Genome Catalog Reveals Extensive Unexplored
1253 Habitat-Specific Microbiome Diversity and Function. *Advanced Science* **10**, 2300050 (2023).
1254 85. Kezic, S. *et al.* Levels of filaggrin degradation products are influenced by both filaggrin
1255 genotype and atopic dermatitis severity. *Allergy* **66**, 934–940 (2011).
1256 86. Hug, D. H., Dunkerson, D. D. & Hunter, J. K. The degradation of l-histidine and *trans* and
1257 *cis*-urocanic acid by bacteria from skin and the role of bacterial *cis*-urocanic acid isomerase.
1258 *Journal of Photochemistry and Photobiology B: Biology* **50**, 66–73 (1999).
1259 87. Walterscheid, J. P. *et al.* Cis-urocanic acid, a sunlight-induced immunosuppressive factor,
1260 activates immune suppression via the 5-HT2A receptor. *Proceedings of the National*
1261 *Academy of Sciences* **103**, 17420–17425 (2006).
1262 88. Marseglia, A. *et al.* Local rhamnosoft, ceramides and L-isoleucine in atopic eczema: a
1263 randomized, placebo controlled trial. *Pediatric Allergy and Immunology* **25**, 271–275 (2014).
1264 89. Chen, H. *et al.* Skin Microbiome, Metabolome and Skin Phenome, from the Perspectives of
1265 Skin as an Ecosystem. *Phenomics* **2**, 363–382 (2022).

1266 90. LEONARDI, R. & JACKOWSKI, S. Biosynthesis of Pantothenic Acid and Coenzyme A.
1267 *EcoSal Plus* **2**, 10.1128/ecosalplus.3.6.3.4 (2007).
1268 91. Zhou, W. *et al.* Skin microbiome attributes associate with biophysical skin aging. *Exp*
1269 *Dermatol* **32**, 1546–1556 (2023).
1270 92. Tauch, A., Fernández-Natal, I. & Soriano, F. A microbiological and clinical review on
1271 *Corynebacterium kroppenstedtii*. *International Journal of Infectious Diseases* **48**, 33–39
1272 (2016).
1273 93. Liu, B. *et al.* IL-33/ST2 signaling excites sensory neurons and mediates itch response in a
1274 mouse model of poison ivy contact allergy. *Proceedings of the National Academy of*
1275 *Sciences* **113**, E7572–E7579 (2016).
1276 94. Trier, A. M. *et al.* IL-33 signaling in sensory neurons promotes dry skin itch. *Journal of*
1277 *Allergy and Clinical Immunology* **149**, 1473-1480.e6 (2022).
1278 95. Leung, M. H. Y., Tong, X., Wilkins, D., Cheung, H. H. L. & Lee, P. K. H. Individual and
1279 household attributes influence the dynamics of the personal skin microbiota and its
1280 association network. *Microbiome* **6**, 1–15 (2018).
1281 96. Tong, X., Leung, M. H. Y., Wilkins, D., Cheung, H. H. L. & Lee, P. K. H. Neutral Processes
1282 Drive Seasonal Assembly of the Skin Mycobiome. *mSystems* **4**, 10.1128/msystems.00004-19
1283 (2019).
1284 97. Seo, J. Y. *et al.* Longitudinal study of the interplay between the skin barrier and facial
1285 microbiome over 1 year. *Front. Microbiol.* **14**, (2023).
1286 98. Jeffery, I. B., Claesson, M. J., O'Toole, P. W. & Shanahan, F. Categorization of the gut
1287 microbiota: enterotypes or gradients? *Nat Rev Microbiol* **10**, 591–592 (2012).
1288 99. Knights, D. *et al.* Rethinking "Enterotypes". *Cell Host Microbe* **16**, 433–437 (2014).

1289 100. Urban, J. *et al.* The effect of habitual and experimental antiperspirant and deodorant product
1290 use on the armpit microbiome. *PeerJ* **4**, e1605 (2016).
1291 101. Zhou, Y. *et al.* Exploration of bacterial community classes in major human habitats.
1292 *Genome Biol* **15**, R66 (2014).
1293 102. Spittaels, K.-J., Ongena, R., Zouboulis, C. C., Crabbé, A. & Coenye, T. Cutibacterium
1294 acnes Phylotype I and II Strains Interact Differently With Human Skin Cells. *Front Cell*
1295 *Infect Microbiol* **10**, 575164 (2020).
1296 103. Conwill, A. *et al.* Anatomy promotes neutral coexistence of strains in the human skin
1297 microbiome. *Cell Host & Microbe* **30**, 171-182.e7 (2022).
1298 104. Severn, M. M. & Horswill, A. R. Staphylococcus epidermidis and its dual lifestyle in skin
1299 health and infection. *Nat Rev Microbiol* **21**, 97–111 (2023).
1300 105. Evans, S. M., Schrlau, A. E., Chalian, A. A., Zhang, P. & Koch, C. J. Oxygen Levels in
1301 Normal and Previously Irradiated Human Skin as Assessed by EF5 Binding. *Journal of*
1302 *Investigative Dermatology* **126**, 2596–2606 (2006).
1303 106. Wong, W. J., Richardson, T., Seykora, J. T., Cotsarelis, G. & Simon, M. C. Hypoxia-
1304 Inducible Factors Regulate Filaggrin Expression and Epidermal Barrier Function. *Journal of*
1305 *Investigative Dermatology* **135**, 454–461 (2015).
1306 107. Cheung, G. Y. C., Joo, H.-S., Chatterjee, S. S. & Otto, M. Phenol-soluble modulins –
1307 critical determinants of staphylococcal virulence. *FEMS microbiology reviews* **38**, 698
1308 (2014).
1309 108. Ch'ng, J.-H. *et al.* Heme cross-feeding can augment *Staphylococcus aureus* and
1310 *Enterococcus faecalis* dual species biofilms. *The ISME Journal* **16**, 2015–2026 (2022).

1311 109. Regina, V. R. *et al.* Decoding scalp health and microbiome dysbiosis in dandruff.
1312 2024.05.02.592279 Preprint at https://doi.org/10.1101/2024.05.02.592279 (2024).
1313 110. Seo, Y., Sung, M., Hwang, J. & Yoon, Y. Minimum Inhibitory Concentration (MIC) of
1314 Propionic Acid, Sorbic Acid, and Benzoic Acid against Food Spoilage Microorganisms in
1315 Animal Products to Use MIC as Threshold for Natural Preservative Production. *Food Sci*
1316 *Anim Resour* **43**, 319–330 (2023).
1317 111. Ianiri, G., LeibundGut-Landmann, S. & Dawson, T. L. Malassezia: A Commensal,
1318 Pathogen, and Mutualist of Human and Animal Skin. *Annual Review of Microbiology* **76**,
1319 757–782 (2022).
1320 112. Hong, C. *et al.* PathoScope 2.0: a complete computational framework for strain
1321 identification in environmental or clinical sequencing samples. *Microbiome* **2**, 33 (2014).
1322 113. Janssens, Y. *et al.* Disbiome database: linking the microbiome to disease. *BMC*
1323 *Microbiology* **18**, 50 (2018).
1324 114. Yao, G. *et al.* MicroPhenoDB Associates Metagenomic Data with Pathogenic Microbes,
1325 Microbial Core Genes, and Human Disease Phenotypes. *Genomics Proteomics*
1326 *Bioinformatics* **18**, 760–772 (2020).
1327 115. de Goffau, M. C. *et al.* Recognizing the reagent microbiome. *Nat Microbiol* **3**, 851–853
1328 (2018).
1329 116. Peschel, S., Müller, C. L., Von Mutius, E., Boulesteix, A.-L. & Depner, M. NetCoMi:
1330 network construction and comparison for microbiome data in R. *Briefings in Bioinformatics*
1331 **22**, bbaa290 (2021).
1332 117. Csárdi, G. *et al.* igraph for R: R interface of the igraph library for graph theory and network
1333 analysis. Zenodo https://doi.org/10.5281/ZENODO.7682609 (2024).

118. Faust, K. *et al.* Microbial Co-occurrence Relationships in the Human Microbiome. *PLOS Computational Biology* **8**, e1002606 (2012).

119. Gill, R., Datta, S. & Datta, S. A statistical framework for differential network analysis from microarray data. *BMC Bioinformatics* **11**, 95 (2010).

120. Chawla, N. V., Bowyer, K. W., Hall, L. O. & Kegelmeyer, W. P. SMOTE: synthetic minority over-sampling technique. *J. Artif. Int. Res.* **16**, 321–357 (2002).

121. Pedregosa, F. *et al.* Scikit-learn: Machine Learning in Python. *Journal of Machine Learning Research* **12**, 2825–2830 (2011).

122. Chen, T. & Guestrin, C. XGBoost: A Scalable Tree Boosting System. in *Proceedings of the 22nd ACM SIGKDD International Conference on Knowledge Discovery and Data Mining* 785–794 (ACM, San Francisco California USA, 2016). doi:10.1145/2939672.2939785.

Figure 1

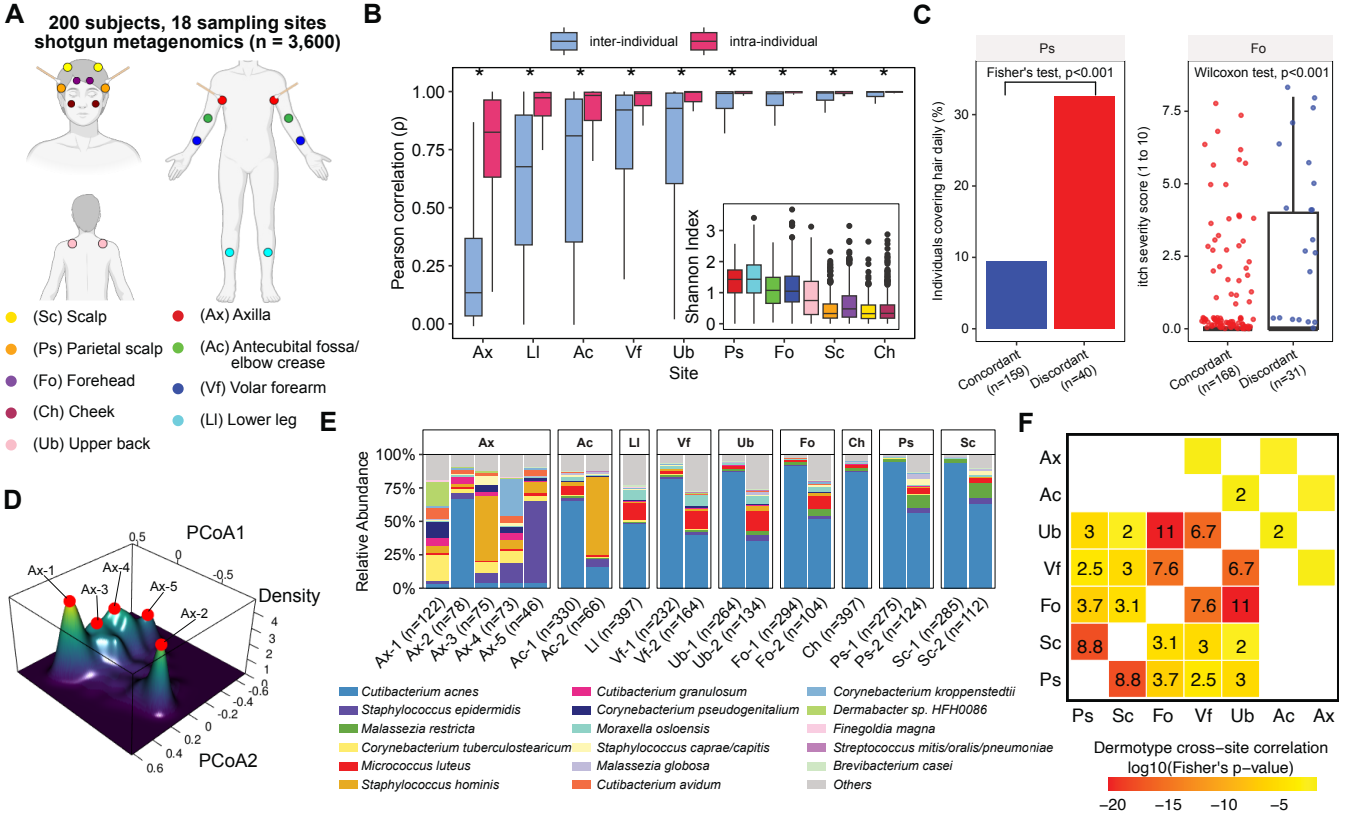
A
200 subjects, 18 sampling sites
shotgun metagenomics (n = 3,600)
(Sc) Scalp
(Ps) Parietal scalp
(Fo) Forehead
(Ch) Cheek
(Ub) Upper back
(Ax) Axilla
(Ac) Antecubital fossa/ elbow crease
(Vf) Volar forearm
(Ll) Lower leg
B
inter-individual
intra-individual
Pearson correlation (ρ)
Shannon Index
Ax
Ll
Ac
Vf
Ub
Ps
Fo
Sc
Ch
Site
C
Ps
Fo
Fisher's test, p<0.001
Wilcoxon test, p<0.001
Individuals covering hair daily (%)
itch severity score (1 to 10)
Concordant (n=159)
Discordant (n=40)
Concordant (n=168)
Discordant (n=31)
D
PCoA1
PCoA2
Density
Ax-1
Ax-2
Ax-3
Ax-4
Ax-5
E
Relative Abundance
Ax-1 (n=122)
Ax-2 (n=78)
Ax-3 (n=75)
Ax-4 (n=73)
Ax-5 (n=46)
Ac-1 (n=330)
Ac-2 (n=66)
Ll (n=397)
Vf-1 (n=232)
Vf-2 (n=164)
Ub-1 (n=264)
Ub-2 (n=134)
Fo-1 (n=294)
Fo-2 (n=104)
Ch (n=397)
Ps-1 (n=275)
Ps-2 (n=124)
Sc-1 (n=285)
Sc-2 (n=112)
Cutibacterium acnes
Cutibacterium granulosum
Corynebacterium kroppenstedtii
Staphylococcus epidermidis
Corynebacterium pseudogenitalium
Dermabacter sp. HFH0086
Malassezia restricta
Moraxella osloensis
Finegoldia magna
Corynebacterium tuberculostearicum
Staphylococcus caprae/capitis
Streptococcus mitis/oralis/pneumoniae
Micrococcus luteus
Malassezia globosa
Brevibacterium casei
Staphylococcus hominis
Cutibacterium avidum
Others
F
Dermotype cross–site correlation
log10(Fisher's p–value)

Figure 2

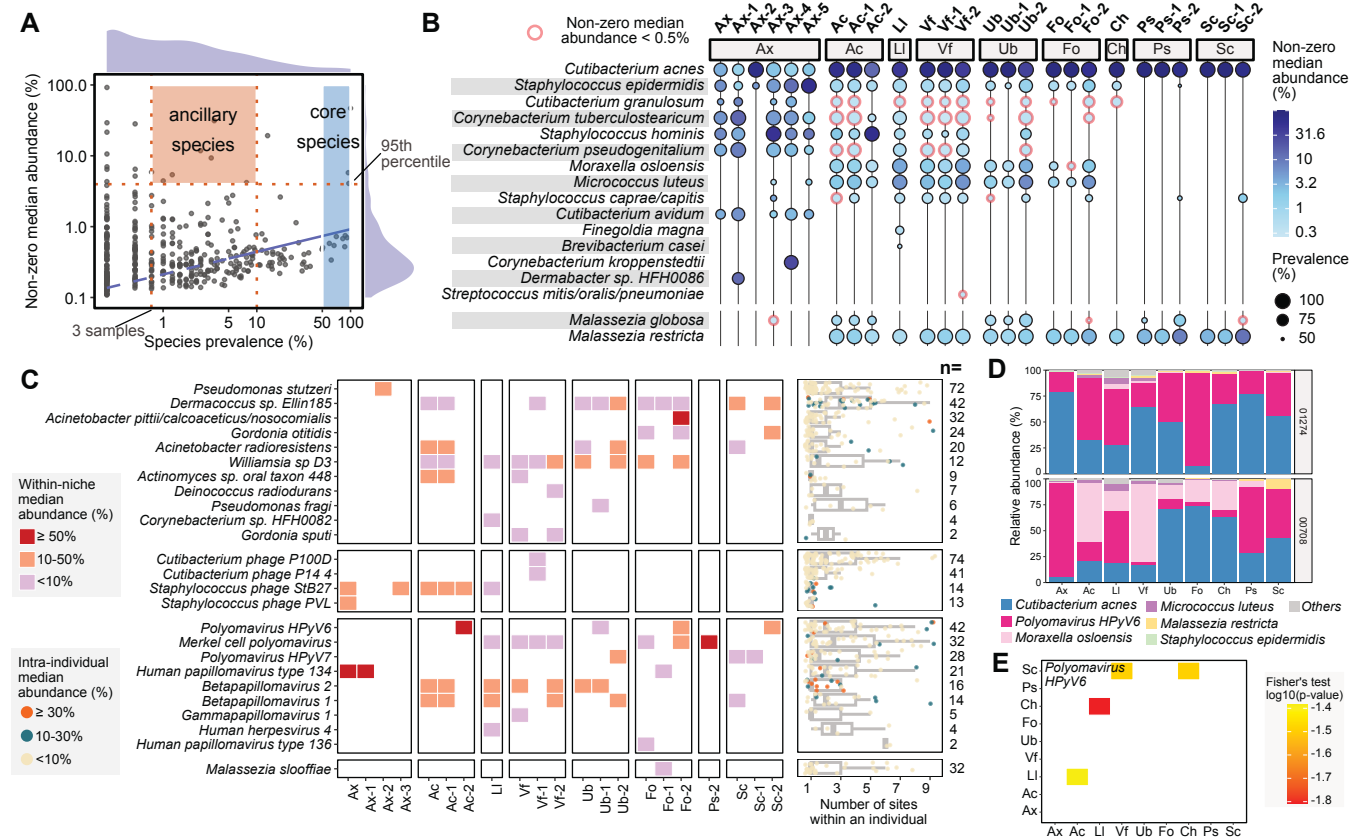
A
Non-zero median abundance (%)
100.0
10.0
1.0
0.1
ancillary species
core species
95th percentile
3 samples
1
5
10
50
100
Species prevalence (%)
B
Non-zero median abundance < 0.5%
Ax
Ac
LI
Vf
Ub
Fo
Ch
Ps
Sc
Cutibacterium acnes
Staphylococcus epidermidis
Cutibacterium granulosum
Corynebacterium tuberculostearicum
Staphylococcus hominis
Corynebacterium pseudogenitalium
Moraxella osloensis
Micrococcus luteus
Staphylococcus caprae/capitis
Cutibacterium avidum
Finegoldia magna
Brevibacterium casei
Corynebacterium kroppenstedtii
Dermabacter sp. HFH0086
Streptococcus mitis/oralis/pneumoniae
Malassezia globosa
Malassezia restricta
Non-zero median abundance (%)
31.6
10
3.2
1
0.3
Prevalence (%)
100
75
50
C
Within-niche median abundance (%)
≥ 50%
10-50%
<10%
Intra-individual median abundance (%)
≥ 30%
10-30%
<10%
Pseudomonas stutzeri
Dermacoccus sp. Ellin185
Acinetobacter pittii/calcoaceticus/nosocomialis
Gordonia otitidis
Acinetobacter radioresistens
Williamsia sp D3
Actinomyces sp. oral taxon 448
Deinococcus radiodurans
Pseudomonas fragi
Corynebacterium sp. HFH0082
Gordonia sputi
Cutibacterium phage P100D
Cutibacterium phage P14 4
Staphylococcus phage StB27
Staphylococcus phage PVL
Polyomavirus HPyV6
Merkel cell polyomavirus
Polyomavirus HPyV7
Human papillomavirus type 134
Betapapillomavirus 2
Betapapillomavirus 1
Gammapapillomavirus 1
Human herpesvirus 4
Human papillomavirus type 136
Malassezia slooffiae
n=
72
42
32
24
20
12
9
7
6
4
2
74
41
14
13
42
32
28
21
16
14
5
4
2
32
Number of sites within an individual
D
Relative abundance (%)
01274
00708
Cutibacterium acnes
Polyomavirus HPyV6
Moraxella osloensis
Micrococcus luteus
Malassezia restricta
Staphylococcus epidermidis
Others
E
Polyomavirus HPyV6
Fisher's test log10(p-value)
-1.4
-1.5
-1.6
-1.7
-1.8

Figure 3

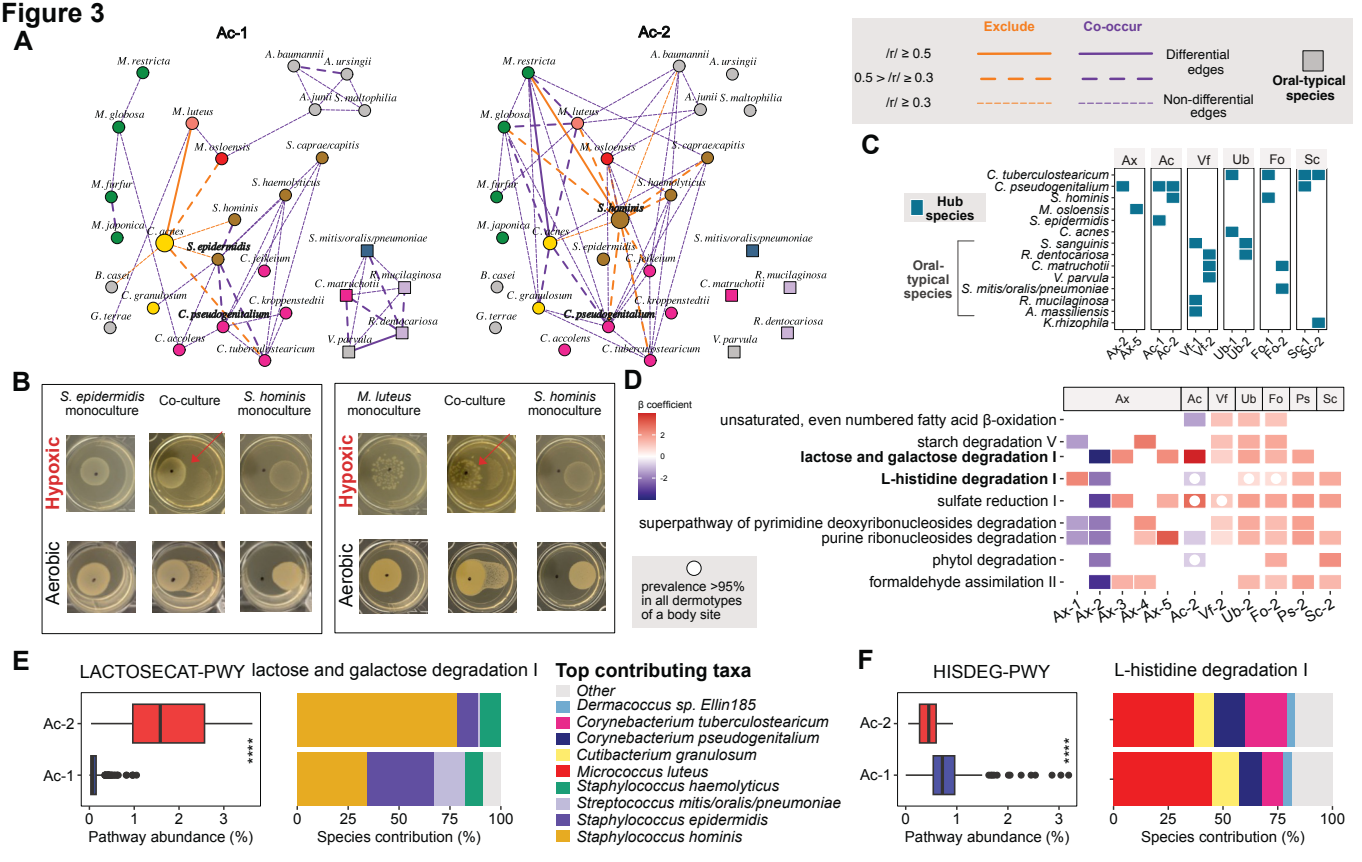
A
Ac-1
Ac-2
M. restricta
A. baumannii
A. ursingii
A. junii
S. maltophilia
M. globosa
M. luteus
M. osloensis
S. caprae/capitis
M. furfur
S. haemolyticus
S. hominis
M. japonica
C. acnes
S. epidermidis
S. mitis/oralis/pneumoniae
C. jeikeium
B. casei
R. mucilaginosa
C. matruchotii
C. granulosum
C. kroppenstedtii
G. terrae
C. pseudogenitalium
R. dentocariosa
C. accolens
C. tuberculostearicum
V. parvula
Exclude
Co-occur
/r/ ≥ 0.5
0.5 > /r/ ≥ 0.3
/r/ ≥ 0.3
Differential edges
Non-differential edges
Oral-typical species
B
S. epidermidis monoculture
Co-culture
S. hominis monoculture
M. luteus monoculture
Hypoxic
Aerobic
C
Hub species
Oral-typical species
Ax
Ac
Vf
Ub
Fo
Sc
C. tuberculostearicum
C. pseudogenitalium
S. hominis
M. osloensis
S. epidermidis
C. acnes
S. sanguinis
R. dentocariosa
C. matruchotii
V. parvula
S. mitis/oralis/pneumoniae
R. mucilaginosa
A. massiliensis
K.rhizophila
Ax-2
Ax-5
Ac-1
Ac-2
Vf-1
Vf-2
Ub-1
Ub-2
Fo-1
Fo-2
Sc-1
Sc-2
D
β coefficient
2
0
-2
prevalence >95% in all dermotypes of a body site
Ax
Ac
Vf
Ub
Fo
Ps
Sc
unsaturated, even numbered fatty acid β-oxidation
starch degradation V
lactose and galactose degradation I
L-histidine degradation I
sulfate reduction I
superpathway of pyrimidine deoxyribonucleosides degradation
purine ribonucleosides degradation
phytol degradation
formaldehyde assimilation II
Ax-1
Ax-2
Ax-3
Ax-4
Ax-5
Ac-2
Vf-2
Ub-2
Fo-2
Ps-2
Sc-2
E
LACTOSECAT-PWY
lactose and galactose degradation I
Ac-2
Ac-1
****
0
1
2
3
Pathway abundance (%)
0
25
50
75
100
Species contribution (%)
Top contributing taxa
Other
Dermacoccus sp. Ellin185
Corynebacterium tuberculostearicum
Corynebacterium pseudogenitalium
Cutibacterium granulosum
Micrococcus luteus
Staphylococcus haemolyticus
Streptococcus mitis/oralis/pneumoniae
Staphylococcus epidermidis
Staphylococcus hominis
F
HISDEG-PWY
L-histidine degradation I
Ac-2
Ac-1
****
0
1
2
3
Pathway abundance (%)
0
25
50
75
100
Species contribution (%)

Figure 4

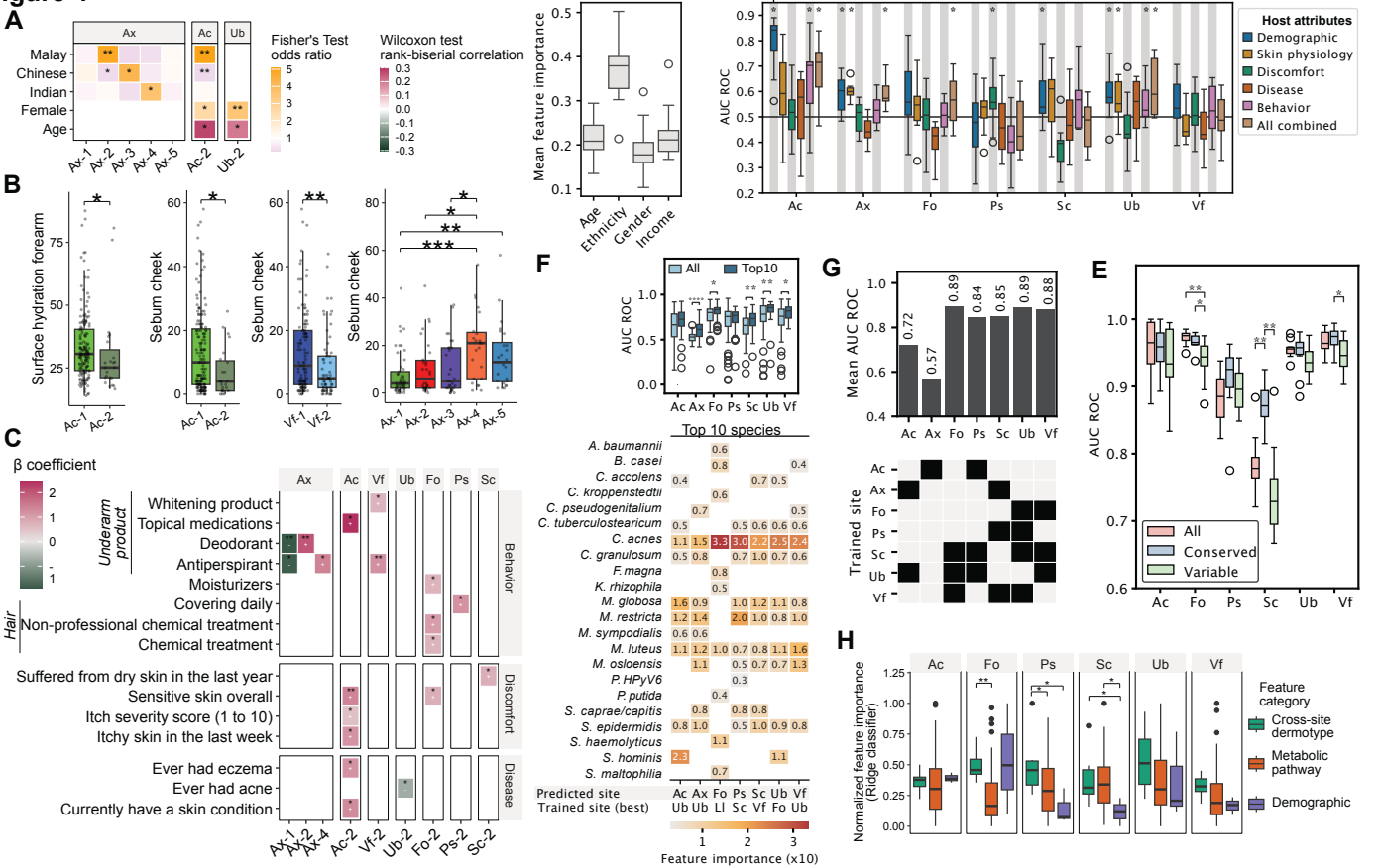
A
Ax
Ac
Ub
Malay
Chinese
Indian
Female
Age
Ax-1
Ax-2
Ax-3
Ax-4
Ax-5
Ac-2
Ub-2
Fisher's Test odds ratio
Wilcoxon test rank-biserial correlation
B
Surface hydration forearm
Sebum cheek
Ac-1
Ac-2
Vf-1
Vf-2
Ax-1
Ax-2
Ax-3
Ax-4
Ax-5
C
β coefficient
Underarm product
Hair
Whitening product
Topical medications
Deodorant
Antiperspirant
Moisturizers
Covering daily
Non-professional chemical treatment
Chemical treatment
Suffered from dry skin in the last year
Sensitive skin overall
Itch severity score (1 to 10)
Itchy skin in the last week
Ever had eczema
Ever had acne
Currently have a skin condition
Behavior
Discomfort
Disease
Ax
Ac
Vf
Ub
Fo
Ps
Sc
D
Mean feature importance
Age
Ethnicity
Gender
Income
AUC ROC
Ac
Ax
Fo
Ps
Sc
Ub
Vf
Host attributes
Demographic
Skin physiology
Discomfort
Disease
Behavior
All combined
F
All
Top10
AUC ROC
Top 10 species
A. baumannii
B. casei
C. accolens
C. kroppenstedtii
C. pseudogenitalium
C. tuberculostearicum
C. acnes
C. granulosum
F. magna
K. rhizophila
M. globosa
M. restricta
M. sympodialis
M. luteus
M. osloensis
P. HPyV6
P. putida
S. caprae/capitis
S. epidermidis
S. haemolyticus
S. hominis
S. maltophilia
Predicted site
Trained site (best)
Ac Ax Fo Ps Sc Ub Vf
Ub Ub Ll Sc Vf Fo Ub
Feature importance (x10)
G
Mean AUC ROC
0.72
0.57
0.89
0.84
0.85
0.89
0.88
Trained site
E
AUC ROC
All
Conserved
Variable
H
Normalized feature importance (Ridge classifier)
Feature category
Cross-site dermotype
Metabolic pathway
Demographic